Computer Methods in Applied Mechanics and Engineering 464 (2027) 119464

Contents lists available at ScienceDirect

Comput. Methods Appl. Mech. Engrg.

journal homepage: www.elsevier.com/locate/cma

Two-and-a-half dimensional complex frequency shifted perfectly matched layers for elastodynamic wave propagation

Stijn François [a,*], Amar Pashov [a], Loukas F. Kallivokas [b], Geert Degrande [a]

[a] KU Leuven, Department of Civil Engineering, Structural Mechanics Section, Kasteelpark Arenberg 40, B-3001 Leuven, Belgium
[b] The University of Texas at Austin, Department of Civil, Architectural and Environmental Engineering, Austin, TX 78712, USA

ARTICLE INFO

Keywords:
Elastodynamics
Wave propagation
Perfectly matched layers
Multi-field finite elements
2.5D PML

ABSTRACT

For the simulation of three-dimensional elastodynamic wave propagation in structures with longitudinally invariant geometry, two-and-a-half dimensional (2.5D) formulations are commonly employed to reduce computational cost by applying a Fourier transform of the longitudinal coordinate into the wavenumber domain. A finite element approach combined with Perfectly Matched Layers (PMLs) enables the absorption of outgoing waves along the boundaries of the computational domain. This paper introduces a 2.5D Complex Frequency Shifted (CFS) PML, in which a frequency shift applied to the PML stretch function enhances wave attenuation, particularly at low frequencies. The formulation uses auxiliary fields that make the system matrices independent of both frequency and wavenumber, thereby eliminating repeated matrix assembly and improving computational performance relative to conventional 2.5D PML techniques. The effectiveness of the proposed 2.5D CFS-PML is demonstrated through several numerical examples, and guidelines for selecting appropriate CFS-PML parameters are discussed.

1. Introduction

In many civil infrastructure systems, the geometry and material properties can be considered invariant along one spatial direction. Typical examples include roads, railway tracks, tunnels, buried pipelines, quay walls, or vibration isolation screens. For such structures, the computational cost of performing three-dimensional (3D) modeling can be greatly reduced by taking advantage of the longitudinal invariance. This naturally leads to a two-and-a-half-dimensional (2.5D) modeling approach [1,2], in which a Fourier transform is applied along the longitudinal direction. As a result, the original 3D problem is reformulated as a sequence of uncoupled two-dimensional (2D) boundary value problems, each associated with a specific longitudinal wavenumber. This strategy enables an efficient description of wave propagation and radiation in unbounded domains. The idea of reducing 3D elastodynamic problems to a family of 2D problems was first introduced by Hwang and Lysmer [1] in their analysis of infinitely long buried structures subjected to traveling seismic waves. The designation *2.5D* was later introduced by Yang and Hung [2], who applied the formulation to the simulation of wave propagation in a half-space induced by moving loads. Since then, 2.5D formulations have become a well-established and widely adopted framework for modeling wave propagation in problems exhibiting longitudinal invariance, and they are now routinely employed in geotechnical applications [3–5] as well as in studies of railway [6–10] and tunnel [11–15] dynamics.

Within the 2.5D framework, several numerical strategies have been developed to enforce the radiation condition associated with wave propagation in unbounded or semi-infinite domains [16,17]. A well-established approach relies on the boundary element

* Corresponding author.
E-mail addresses: stijn.francois@kuleuven.be (S. François), amar.pashov@kuleuven.be (A. Pashov), loukas@mail.utexas.edu (L.F. Kallivokas), geert.degrande@kuleuven.be (G. Degrande).

https://doi.org/10.1016/j.cma.2026.119464
Received 18 May 2026; Received in revised form 10 September 2026; Accepted 27 September 2026
0045-7825/© 2026 Elsevier B.V. All rights are reserved, including those for text and data mining, AI training, and similar technologies.

(BE) method, either as a standalone formulation [18,19] or in coupled finite element–boundary element (FE–BE) schemes [20–22]. In 2.5D BE methods, the unbounded domain is modeled analytically using 2.5D Green's functions [23,24], which yield an exact representation of wave radiation at infinity. Despite their high accuracy, BE methods typically lead to fully populated system matrices [25–27]. This results in substantial computational cost and memory requirements, which become particularly restrictive for large-scale models, high-frequency analyses, or parametric studies involving multiple frequencies or wavenumbers [28].

Another family of approaches employs infinite or absorbing finite elements [29]. These methods extend the computational domain by introducing shape functions that gradually diminish in amplitude and vanish asymptotically at infinity [30,31]. However, their accuracy may deteriorate in the presence of complex wave fields, evanescent modes, or waves impinging at grazing incidence [32,33].

As an alternative, Perfectly Matched Layers (PMLs) have emerged as a robust and versatile alternative for modeling radiation conditions in elastodynamic problems [34]. PMLs attenuate outgoing waves without reflection by introducing a complex coordinate stretching within an artificial buffer zone surrounding the domain of interest [35]. In problems exhibiting longitudinal invariance, this concept has been successfully incorporated into 2.5D formulations [36,37]. These methods combine the efficiency of the 2.5D framework with the strong absorption properties of PMLs, enabling accurate simulation of wave propagation towards infinity.

The selection between 2.5D FE–BE and 2.5D FE–PML approaches is guided by the geometry under consideration and the aims of the analysis. FE–BE techniques are especially beneficial when the BE mesh is relatively small, e.g. for surface footings or shallow structural systems, and when accurately capturing wave propagation over large distances is a primary requirement. Conversely, FE–PML approaches are better suited for embedded foundations, such as pile groups or deep structures, which would typically require large BE meshes, or in cases where the primary focus is the calculation of the structural response rather than the radiated wave field. PML formulations maintain sparse matrices, offering computational efficiency for large-scale models.

A key limitation of the available 2.5D PML formulations is that the resulting system matrices depend explicitly on the longitudinal wavenumber and the frequency [36]. Consequently, the global stiffness matrix has to be reassembled for every wavenumber and frequency under consideration, which introduces substantial computational overhead and restricts the efficiency of the method in applications such as dispersion analysis, broadband excitation, or reduced-order modeling.

Furthermore, standard PML stretching functions are used, which are known to exhibit insufficient attenuation at low frequencies, particularly for evanescent waves or waves propagating at grazing incidence [38]. To overcome the latter deficiency, the Complex Frequency Shifted (CFS) PML was introduced in the context of 2D and 3D elastic wave propagation as an enhanced formulation that improves both numerical stability and absorption performance [39,40]. By introducing a complex frequency shift in the coordinate stretching, the CFS-PML significantly enhances the attenuation of evanescent and low-frequency waves while maintaining stability [41–43] in transient calculations. For 2D transient analyses, a CFS-PML formulation was recently developed [44], where the resulting discretized equations, obtained through the introduction of auxiliary fields [45], retain the standard second-order form commonly used in structural dynamics, i.e. a form characterized by stiffness, damping, and mass matrices. This structure allows the use of conventional time integration schemes and facilitates coupling with (commercial) finite element solvers.

The main contribution of this paper is the development of a 2.5D CFS-PML formulation for elastodynamic wave propagation in unbounded domains. The present work extends the 2.5D displacement-based PML formulation of François et al. [36] through the incorporation of a complex frequency shift (CFS) and an auxiliary-field reformulation of the governing equations, inspired by [44]. As formulated, these system matrices need to be assembled only once, eliminating the repeated reassembly required in conventional displacement-based 2.5D PML formulations [36]. Frequency- and wavenumber-independent system matrices enable the evaluation of dispersion curves via quadratic eigenvalue problems [46], and make the approach well suited for model order-reduction techniques [47]. This yields a flexible and efficient alternative to conventional 2.5D FE–BE formulations for computing dynamic soil–structure interaction in longitudinally invariant problems.

The remainder of this paper is organized as follows. Section 2 introduces the problem formulation and the complex-frequency-shifted stretching functions. Section 3 presents the governing equations of the CFS-PML in weak form, and its finite element discretization using a Galerkin approach. Section 4 presents verification tests and numerical examples. First, the one-dimensional (1D) wave propagation solution in a semi-infinite bar is analytically derived and solved with the proposed CFS-PML formulation. Next, 2D wave propagation in a homogeneous halfspace is computed and compared with a reference solution to assess wave absorption of the CFS-PML under varying angles of incidence. Subsequently, the dynamic soil–structure interaction between a cut-and-cover tunnel and the soil is computed as an application of the proposed method in 2.5D. Section 5 summarizes the main conclusions of the paper.

2. Formulation of the CFS-PML

2.1. Problem geometry

Fig. 1 shows a linear elastic domain Ω, which is invariant in the longitudinal direction y. The domain Ω consists of an interior domain Ω_{ID} and a PML buffer layer Ω_{PML} placed at its edges to absorb outgoing waves propagating in the directions x and z.

Apart from the assumptions inherent to the 2.5D finite element formulation, including linear elastic behavior, no additional restrictions are imposed on the interior domain Ω_{ID} by the PML formulation itself. Consequently, the interior domain may have an arbitrary cross-section and may comprise heterogeneous or (an)isotropic materials, provided that they can be represented within a linear 2.5D finite element model [36,48]. Likewise, different finite element technologies, such as continuum, beam, shell, and interface elements, may be employed.

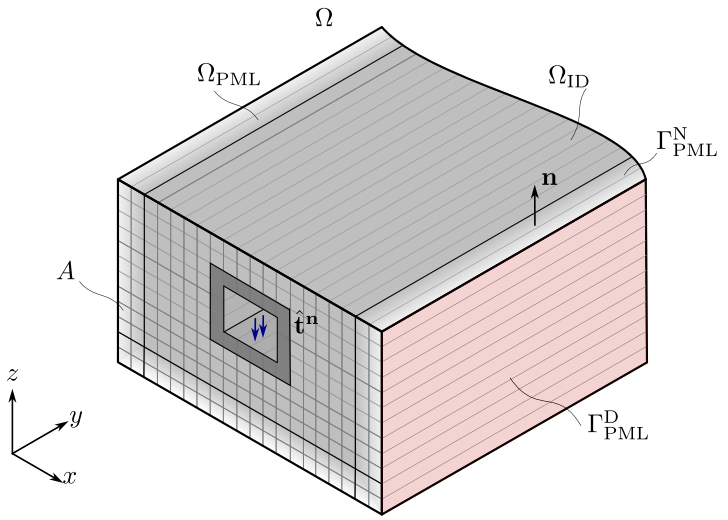

Fig. 1. 3D domain Ω with an invariant cross-section A, terminated by a PML Ω_{PML} surrounding the physical interior domain Ω_{ID}.

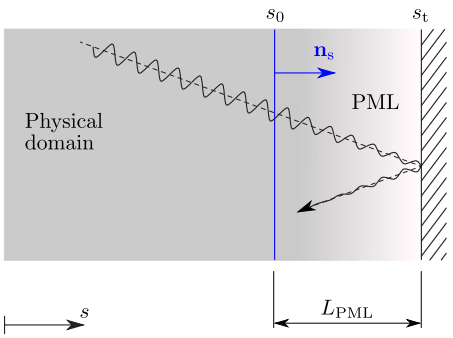

Fig. 2. PML domain in the direction of coordinate s. The waves pass through the interface s_0 without reflections, and decay with distance within the PML.

2.2. The CFS-PML stretching functions

The PML achieves its non-reflecting property through a complex coordinate transformation, in which the spatial coordinates x and z are transformed into complex-valued stretched coordinates $\tilde{x}$ and $\tilde{z}$ [35,49]. For a generic coordinate $s \in \{x, z\}$, this mapping is defined as

$$s \mapsto \tilde{s} = s_0 + \int_{s_0}^{s} \lambda_s(s', \omega)\, \mathrm{d}s', \tag{1}$$

where s_0 denotes the interface between the physical domain and the PML region, $\tilde{s}$ is the stretched coordinate, and $\lambda_s(s, \omega)$ is the complex stretch function (Fig. 2). The PML is terminated at the coordinate $s = s_{\mathrm{t}}$. Differentiation of the mapping (1) with respect to the physical coordinate yields

$$\frac{\mathrm{d}\tilde{s}}{\mathrm{d}s} = \frac{\mathrm{d}}{\mathrm{d}s} \int_{s_0}^{s} \lambda_s(s', \omega)\, \mathrm{d}s' = \lambda_s(s, \omega), \tag{2}$$

which shows that the stretch function governs the local scaling of the coordinate transformation. Consequently, spatial derivatives with respect to the stretched coordinate $\tilde{s}$ can be related to derivatives with respect to the physical coordinate s according to

$$\frac{\mathrm{d}}{\mathrm{d}\tilde{s}} = \frac{1}{\lambda_s(s, \omega)} \frac{\mathrm{d}}{\mathrm{d}s}. \tag{3}$$

This relation allows the PML to be incorporated into the governing equations by modifying the differential operators or, equivalently, by introducing complex-valued effective material parameters [50].

A commonly adopted choice for the stretch function is the standard PML formulation, defined as:

$$\lambda_s(s,\omega) = \alpha_s(s) + \frac{\beta_s(s)}{\mathrm{i}\omega}, \tag{4}$$

where $\alpha_s(s)$ and $\beta_s(s)$ are real-valued, smoothly varying functions within the PML region [51]. The first term $\alpha_s(s)$ produces a real coordinate stretching, while the second term, controlled by $\beta_s(s)$, introduces frequency-dependent attenuation. As a result, outgoing waves decay exponentially inside the PML without reflection at the interface s_0 with the physical domain.

In order to enhance the absorption performance of the perfectly matched layer, particularly at low frequencies and for waves at grazing incidence, the CFS-PML formulation introduces an additional frequency shift into the stretch function [39]. This modification alleviates the poor performance of the standard PML at low frequencies. The CFS-PML stretch function is defined as

$$\lambda_s(s,\omega) = \alpha_s(s) + \frac{\beta_s(s)}{\omega_s(s) + \mathrm{i}\omega}, \tag{5}$$

where ω_s is a real, positive frequency shift parameter. By shifting the pole of the stretching function away from the origin in the complex frequency plane, this formulation ensures effective damping of low-frequency components and significantly reduces spurious reflections for waves propagating nearly parallel to the PML interface. As a result, the CFS-PML provides more robust and broadband absorption compared to the standard PML formulation given in Eq. (4) [39].

The buffer zone remains perfectly matched, and therefore non-reflecting, provided that the stretch function equals unity at the interface $s = s_0$ between the physical domain Ω_{ID} and the absorbing layer Ω_{PML}:

$$\lambda_s(s_0,\omega) = 1, \quad \forall\omega. \tag{6}$$

This condition is satisfied by prescribing the following spatial profiles for the stretching parameters

$$\alpha_s(s) = 1 + \alpha_0 \left[\frac{(s-s_0)n_s}{L_{\mathrm{PML}}}\right]^{m_0} \tag{7}$$

and

$$\beta_s(s) = \beta_0 \left[\frac{(s-s_0)n_s}{L_{\mathrm{PML}}}\right]^{m_0}, \tag{8}$$

where α_0 and β_0 are scaling parameters that control the strength of the coordinate stretching, and attenuation, respectively, L_{PML} denotes the thickness of the PML in the considered coordinate direction (Fig. 2), and $n_s = \pm 1$ defines the outward normal direction of the layer. The exponent m_0 specifies the polynomial order of the spatial grading and governs the smoothness of the transition from the physical domain into the absorbing layer.

In the CFS-PML formulation, a similar spatial grading can be adopted for the frequency-shift parameter $\omega_s(s)$ [52]:

$$\omega_s(s) = \omega_0 \left[1 - \left(\frac{(s-s_0)n_s}{L_{\mathrm{PML}}}\right)^{m_2}\right], \tag{9}$$

where ω_0 is the reference frequency shift at the interface, such that $\omega_s(s = s_0) = \omega_0$, and m_2 denotes the polynomial degree controlling the spatial variation of the frequency shift within the PML.

2.3. Governing equations in the interior domain Ω_{ID}

Within the internal domain Ω_{ID}, the 3D dynamic equilibrium of the elastic medium in the frequency domain is governed by

$$\mathbf{L}^{\mathrm{T}}\hat{\boldsymbol{\sigma}} + \rho\omega^2\hat{\mathbf{u}} = \mathbf{0}, \tag{10}$$

where $\hat{\boldsymbol{\sigma}} = \{\hat{\sigma}_{xx}, \hat{\sigma}_{yy}, \hat{\sigma}_{zz}, \hat{\sigma}_{xy}, \hat{\sigma}_{yz}, \hat{\sigma}_{zx}\}^{\mathrm{T}}$ is the stress vector and $\hat{\mathbf{u}} = \{\hat{u}_x, \hat{u}_y, \hat{u}_z\}^{\mathrm{T}}$ collects the displacement vector components, ρ denotes the mass density, ω is the angular frequency, and $\square^{\mathrm{T}}$ represents a transpose. A superposed hat indicates the Fourier transform of the corresponding time-domain quantity. Both $\hat{\boldsymbol{\sigma}}$ and $\hat{\boldsymbol{u}}$ depend on the spatial coordinates $\boldsymbol{x} = (x, y, z)$ and on the frequency ω; this functional dependence is omitted for brevity. The differential operator matrix $\mathbf{L}$ appearing in Eq. (10) is defined as

$$\mathbf{L}^{\mathrm{T}} = \begin{bmatrix} \frac{\partial}{\partial x} & 0 & 0 & \frac{\partial}{\partial y} & 0 & \frac{\partial}{\partial z} \\ 0 & \frac{\partial}{\partial y} & 0 & \frac{\partial}{\partial x} & \frac{\partial}{\partial z} & 0 \\ 0 & 0 & \frac{\partial}{\partial z} & 0 & \frac{\partial}{\partial y} & \frac{\partial}{\partial x} \end{bmatrix}, \tag{11}$$

which represents the divergence in Voigt notation.

The strain vector $\hat{\boldsymbol{\epsilon}} = \{\hat{\epsilon}_{xx}, \hat{\epsilon}_{yy}, \hat{\epsilon}_{zz}, \hat{\gamma}_{xy}, \hat{\gamma}_{yz}, \hat{\gamma}_{zx}\}^{\mathrm{T}}$, where $\hat{\gamma}_{xy}$, $\hat{\gamma}_{yz}$, and $\hat{\gamma}_{zx}$ denote the engineering shear strains, is defined through the kinematic relations

$$\hat{\boldsymbol{\epsilon}} = \mathbf{L}\,\hat{\mathbf{u}}, \tag{12}$$

For a linear, homogeneous, isotropic elastic medium, the constitutive relation is given by

$$\hat{\boldsymbol{\sigma}} = \mathbf{C}\,\hat{\boldsymbol{\epsilon}}, \tag{13}$$

with $\mathbf{C}$ the elasticity matrix expressed in terms of the Lamé parameters λ and μ,

$$\mathbf{C} = \begin{bmatrix} \lambda+2\mu & \lambda & \lambda & 0 & 0 & 0 \\ \lambda & \lambda+2\mu & \lambda & 0 & 0 & 0 \\ \lambda & \lambda & \lambda+2\mu & 0 & 0 & 0 \\ 0 & 0 & 0 & \mu & 0 & 0 \\ 0 & 0 & 0 & 0 & \mu & 0 \\ 0 & 0 & 0 & 0 & 0 & \mu \end{bmatrix}. \tag{14}$$

2.4. Governing equations in the PML buffer Ω_{PML}

Within the PML buffer Ω_{PML}, wave attenuation is achieved by transforming the governing equilibrium equations through the complex coordinate mapping. Specifically, the transformation is applied to the spatial derivatives appearing in the differential operator matrix $\mathbf{L}$ by successively setting $s = x$ and $s = z$ in the coordinate stretching (Eq. (1)). As a result, derivatives with respect to the physical coordinates are replaced by derivatives with respect to the stretched coordinates, introducing the inverse stretch functions $1/\lambda_x$ and $1/\lambda_z$ in the corresponding directions, whereas no stretching is applied in the y-direction. As a result, the stretch functions are not dependent on the longitudinal coordinate y. Applying this transformation to the equilibrium Eq. (10) yields the modified system

$$\left(\frac{1}{\lambda_x}\mathbf{L}_x + \mathbf{L}_y + \frac{1}{\lambda_z}\mathbf{L}_z\right)^{\mathrm{T}} \hat{\boldsymbol{\sigma}} + \rho\omega^2 \hat{\mathbf{u}} = \mathbf{0}, \tag{15}$$

where the matrices of differential operators $\mathbf{L}_x$, $\mathbf{L}_y$, and $\mathbf{L}_z$ isolate the contributions associated with differentiation in the x-, y-, and z-directions, respectively. They are defined as

$$\mathbf{L}_x = \mathbf{L}_{x0}\frac{\partial}{\partial x}, \qquad \mathbf{L}_y = \mathbf{L}_{y0}\frac{\partial}{\partial y}, \text{ and} \qquad \mathbf{L}_z = \mathbf{L}_{z0}\frac{\partial}{\partial z}, \tag{16}$$

where the constant selection matrices $\mathbf{L}_{x0}$, $\mathbf{L}_{y0}$, and $\mathbf{L}_{z0}$ specify how each directional derivative contributes to the divergence of the stress tensor in Voigt notation. They are given by

$$\mathbf{L}_{x0}^{\mathrm{T}} = \begin{bmatrix} 1&0&0&0&0&0 \\ 0&0&0&1&0&0 \\ 0&0&0&0&0&1 \end{bmatrix}, \ \mathbf{L}_{y0}^{\mathrm{T}} = \begin{bmatrix} 0&0&0&1&0&0 \\ 0&1&0&0&0&0 \\ 0&0&0&0&1&0 \end{bmatrix}, \quad \text{and} \quad \mathbf{L}_{z0}^{\mathrm{T}} = \begin{bmatrix} 0&0&0&0&0&1 \\ 0&0&0&0&1&0 \\ 0&0&1&0&0&0 \end{bmatrix}. \tag{17}$$

The operator $\mathbf{L}$ can hence be decomposed as

$$\mathbf{L} = \mathbf{L}_x + \mathbf{L}_y + \mathbf{L}_z. \tag{18}$$

To obtain a more convenient form of the governing equations for numerical implementation, the transformed equilibrium Eq. (15) is multiplied by the product of the stretch functions $\lambda_x\lambda_z$. This removes the denominators associated with the stretched derivatives and leads to

$$\left(\lambda_z\mathbf{L}_x + \lambda_x\lambda_z\mathbf{L}_y + \lambda_x\mathbf{L}_z\right)^{\mathrm{T}} \hat{\boldsymbol{\sigma}} + \rho\lambda_x\lambda_z\omega^2\hat{\mathbf{u}} = \mathbf{0}, \tag{19}$$

where the effect of the PML now appears as complex-valued, spatially varying coefficients multiplying the differential operators and the inertia term. In an analogous manner, the kinematic relations (12) are transformed under complex coordinate stretching. The resulting strain–displacement relation in the PML domain reads

$$\hat{\boldsymbol{\epsilon}} = \left(\frac{1}{\lambda_x}\mathbf{L}_x + \mathbf{L}_y + \frac{1}{\lambda_z}\mathbf{L}_z\right)\hat{\mathbf{u}}. \tag{20}$$

2.5. Boundary and interface conditions

The governing equations for the boundary value problem defined in the interior domain Ω_{ID} and in the surrounding PML buffer Ω_{PML} are accompanied by suitable boundary and interface conditions. On the outer boundary of the PML, denoted as $\Gamma^{\text{D}}_{\text{PML}}$, a homogeneous Dirichlet condition is imposed in order to truncate the computational domain, such that

$$\hat{\mathbf{u}} = \mathbf{0}, \quad \mathbf{x} \in \Gamma^{\text{D}}_{\text{PML}}. \tag{21}$$

This condition is admissible since the PML ensures that outgoing waves are sufficiently attenuated before reaching the exterior boundary.

On the remaining boundary of the PML buffer, corresponding to a traction-free surface $\Gamma^{\text{N}}_{\text{PML}}$, the natural boundary condition takes the form

$$\lambda_x\lambda_z\hat{\mathbf{t}}^{\mathbf{n}} = \mathbf{0}, \quad \mathbf{x} \in \Gamma^{\text{N}}_{\text{PML}}, \tag{22}$$

where the factors λ_x and λ_z arise from the coordinate stretching and ensure consistency of the traction condition within the PML formulation.

The traction vector $\hat{\mathbf{t}}^{\mathbf{n}}$ associated with an outward unit normal $\mathbf{n} = \{n_x, n_z\}^{\mathrm{T}}$ is defined as

$$\hat{\mathbf{t}}^{\mathbf{n}} = \begin{bmatrix} \hat{\sigma}_{xx} n_x + \hat{\sigma}_{zx} n_z \\ \hat{\sigma}_{xy} n_x + \hat{\sigma}_{yz} n_z \\ \hat{\sigma}_{xz} n_x + \hat{\sigma}_{zz} n_z \end{bmatrix}. \tag{23}$$

On the free surface of the interior domain, denoted as $\Gamma_{\mathrm{ID}}^{\mathrm{N}}$, the traction vector vanishes except on the portion $\Gamma_{\mathrm{ID}}^{\mathrm{L}} \subset \Gamma_{\mathrm{ID}}^{\mathrm{N}}$ where external loading is applied. Accordingly, the boundary conditions read

$$\hat{\mathbf{t}}^{\mathbf{n}} = \mathbf{0}, \qquad \mathbf{x} \in \Gamma_{\mathrm{ID}}^{\mathrm{N}} \setminus \Gamma_{\mathrm{ID}}^{\mathrm{L}}, \tag{24}$$

and

$$\hat{\mathbf{t}}^{\mathbf{n}} = \hat{\mathbf{p}}_{0,\mathrm{ID}}, \qquad \mathbf{x} \in \Gamma_{\mathrm{ID}}^{\mathrm{L}}, \tag{25}$$

where $\hat{\mathbf{p}}_{0,\mathrm{ID}}$ denotes the prescribed traction applied on $\Gamma_{\mathrm{ID}}^{\mathrm{L}}$.

Finally, on the interface Γ_{I} separating the interior domain from the PML buffer, continuity of displacements and equilibrium of tractions must be enforced. These interface conditions are expressed as

$$\hat{\mathbf{u}}\Big|_{\Gamma_{\mathrm{I}}^{-}} = \hat{\mathbf{u}}\Big|_{\Gamma_{\mathrm{I}}^{+}}, \quad \text{and} \quad \hat{\mathbf{t}}^{\mathbf{n}}\Big|_{\Gamma_{\mathrm{I}}^{-}} = -\hat{\mathbf{t}}^{\mathbf{n}}\Big|_{\Gamma_{\mathrm{I}}^{+}}, \tag{26}$$

where the superscripts $\square^{-}$ and $\square^{+}$ denote the limits approaching the interface from the interior domain Ω_{ID} and the PML buffer Ω_{PML}, respectively. The sign change in the traction condition reflects the opposite orientations of the outward unit normals on either side of the interface, so that the tractions are in equilibrium.

2.6. Weak forms

Following the standard Galerkin weighted residual procedure, the frequency-domain equilibrium Eqs. (10) are first multiplied by kinematically admissible test functions $\hat{\mathbf{v}}$ and subsequently integrated over the interior domain Ω_{ID}. After applying integration by parts and invoking the divergence theorem, the weak form of the equilibrium equations in the interior domain is obtained as

$$\int_{\Omega_{\mathrm{ID}}} \left(\mathbf{L}\hat{\mathbf{v}}\right)^{\mathrm{T}} \hat{\boldsymbol{\sigma}} \, \mathrm{d}V - \omega^2 \int_{\Omega_{\mathrm{ID}}} \rho \hat{\mathbf{v}}^{\mathrm{T}} \hat{\mathbf{u}} \, \mathrm{d}V = \int_{\Gamma_{\mathrm{I}}} \hat{\mathbf{v}}^{\mathrm{T}} \hat{\mathbf{t}}^{\mathbf{n}} \, \mathrm{d}A + \int_{\Gamma_{\mathrm{ID}}^{\mathrm{L}}} \hat{\mathbf{v}}^{\mathrm{T}} \hat{\mathbf{p}}_{0,\mathrm{ID}} \, \mathrm{d}A, \tag{27}$$

where the boundary terms arise naturally from the integration by parts.

The equilibrium equations in the PML buffer Ω_{PML}, given by Eq. (19), are treated in an analogous way. Taking into account the boundary conditions (21)–(22), the corresponding weak form reads

$$\int_{\Omega_{\mathrm{PML}}} \left(\lambda_z \mathbf{L}_x \hat{\mathbf{v}} + \lambda_x \lambda_z \mathbf{L}_y \hat{\mathbf{v}} + \lambda_x \mathbf{L}_z \hat{\mathbf{v}}\right)^{\mathrm{T}} \hat{\boldsymbol{\sigma}} \, \mathrm{d}V - \omega^2 \int_{\Omega_{\mathrm{PML}}} \rho \lambda_x \lambda_z \hat{\mathbf{v}}^{\mathrm{T}} \hat{\mathbf{u}} \, \mathrm{d}V = - \int_{\Gamma_{\mathrm{I}}} \lambda_x \lambda_z \hat{\mathbf{v}}^{\mathrm{T}} \hat{\mathbf{t}}^{\mathbf{n}} \, \mathrm{d}A. \tag{28}$$

Due to the matching condition (6), it follows that $\lambda_x = \lambda_z = 1$ on the interface Γ_{I}.

By adding (27) and (28), and noting that the interface traction terms cancel as a consequence of the continuity conditions (26), the weak form over the entire computational domain $\Omega_{\mathrm{ID}} \cup \Omega_{\mathrm{PML}}$ is obtained:

$$\begin{aligned} &\int_{\Omega_{\mathrm{ID}}} \left(\mathbf{L}\hat{\mathbf{v}}\right)^{\mathrm{T}} \hat{\boldsymbol{\sigma}} \, \mathrm{d}V - \omega^2 \int_{\Omega_{\mathrm{ID}}} \rho \hat{\mathbf{v}}^{\mathrm{T}} \hat{\mathbf{u}} \, \mathrm{d}V + \int_{\Omega_{\mathrm{PML}}} \left(\lambda_z \mathbf{L}_x \hat{\mathbf{v}} + \lambda_x \lambda_z \mathbf{L}_y \hat{\mathbf{v}} + \lambda_x \mathbf{L}_z \hat{\mathbf{v}}\right)^{\mathrm{T}} \hat{\boldsymbol{\sigma}} \, \mathrm{d}V \\ &- \omega^2 \int_{\Omega_{\mathrm{PML}}} \rho \lambda_x \lambda_z \hat{\mathbf{v}}^{\mathrm{T}} \hat{\mathbf{u}} \, \mathrm{d}V = \int_{\Gamma_{\mathrm{ID}}^{\mathrm{L}}} \hat{\mathbf{v}}^{\mathrm{T}} \hat{\mathbf{p}}_{0,\mathrm{ID}} \, \mathrm{d}A. \end{aligned} \tag{29}$$

Upon substitution of the constitutive relation (13) and kinematic relations (12) into (29), followed by the introduction of standard FE approximations for the trial field $\hat{\mathbf{u}}$ and the test field $\hat{\mathbf{v}}$, the first two terms in (29) yield the standard 2.5D stiffness and consistent mass contributions associated with a displacement-based elastodynamic formulation on the interior domain [36]. These contributions are collected in the dynamic stiffness operator $\hat{\mathbf{S}}_{\mathrm{ID}}$, defined as

$$\hat{\mathbf{S}}_{\mathrm{ID}} = \int_{\Omega_{\mathrm{ID}}} \left(\mathbf{L}\hat{\mathbf{v}}\right)^{\mathrm{T}} \hat{\boldsymbol{\sigma}} \, \mathrm{d}V - \omega^2 \int_{\Omega_{\mathrm{ID}}} \rho \hat{\mathbf{v}}^{\mathrm{T}} \hat{\mathbf{u}} \, \mathrm{d}V. \tag{30}$$

The remaining terms from the left hand side of Eq. (29) are defined exclusively over the PML buffer Ω_{PML} and are therefore collected into the generalized PML dynamic stiffness operator $\hat{\mathbf{S}}_{\mathrm{PML}}$, given by

$$\hat{\mathbf{S}}_{\mathrm{PML}} = \int_{\Omega_{\mathrm{PML}}} \left(\lambda_z \mathbf{L}_x \hat{\mathbf{v}} + \lambda_x \lambda_z \mathbf{L}_y \hat{\mathbf{v}} + \lambda_x \mathbf{L}_z \hat{\mathbf{v}}\right)^{\mathrm{T}} \hat{\boldsymbol{\sigma}} \, \mathrm{d}V - \omega^2 \int_{\Omega_{\mathrm{PML}}} \rho \lambda_x \lambda_z \hat{\mathbf{v}}^{\mathrm{T}} \hat{\mathbf{u}} \, \mathrm{d}V. \tag{31}$$

Introducing the stretched kinematic relations (20) into (31) yields:

$$\hat{\mathbf{S}}_{\mathrm{PML}} = \int_{\Omega_{\mathrm{PML}}} \left(\lambda_z \mathbf{L}_x \hat{\mathbf{v}} + \lambda_x \lambda_z \mathbf{L}_y \hat{\mathbf{v}} + \lambda_x \mathbf{L}_z \hat{\mathbf{v}}\right)^{\mathrm{T}} \mathbf{C} \left(\frac{1}{\lambda_x}\mathbf{L}_x + \mathbf{L}_y + \frac{1}{\lambda_z}\mathbf{L}_z\right) \hat{\mathbf{u}} \, \mathrm{d}V - \omega^2 \int_{\Omega_{\mathrm{PML}}} \rho \lambda_x \lambda_z \hat{\mathbf{v}}^{\mathrm{T}} \hat{\mathbf{u}} \, \mathrm{d}V, \tag{32}$$

which can be expanded into:

$$\hat{\mathbf{S}}_{\mathrm{PML}} = \int_{\Omega_{\mathrm{PML}}} \left[\frac{\lambda_z}{\lambda_x} \left(\mathbf{L}_x \hat{\mathbf{v}}\right)^{\mathrm{T}} \mathbf{C} \mathbf{L}_x + \lambda_x \lambda_z \left(\mathbf{L}_y \hat{\mathbf{v}}\right)^{\mathrm{T}} \mathbf{C} \mathbf{L}_y + \frac{\lambda_x}{\lambda_z} \left(\mathbf{L}_z \hat{\mathbf{v}}\right)^{\mathrm{T}} \mathbf{C} \mathbf{L}_z + \right.$$

$$\lambda_z\left(\left(\mathbf{L}_x\hat{\mathbf{v}}\right)^{\mathrm{T}}\mathbf{C}\mathbf{L}_y+\left(\mathbf{L}_y\hat{\mathbf{v}}\right)^{\mathrm{T}}\mathbf{C}\mathbf{L}_x\right)+\lambda_x\left(\left(\mathbf{L}_z\hat{\mathbf{v}}\right)^{\mathrm{T}}\mathbf{C}\mathbf{L}_y+\left(\mathbf{L}_y\hat{\mathbf{v}}\right)^{\mathrm{T}}\mathbf{C}\mathbf{L}_z\right)+$$
$$\left(\mathbf{L}_x\hat{\mathbf{v}}\right)^{\mathrm{T}}\mathbf{C}\mathbf{L}_z+\left(\mathbf{L}_z\hat{\mathbf{v}}\right)^{\mathrm{T}}\mathbf{C}\mathbf{L}_x\Big]\hat{\mathbf{u}}\,\mathrm{d}V-\omega^2\int_{\Omega_{\mathrm{PML}}}\rho\lambda_x\lambda_z\hat{\mathbf{v}}^{\mathrm{T}}\hat{\mathbf{u}}\,\mathrm{d}V. \tag{33}$$

After discretization, Eq. (33) involves displacement degrees of freedom associated exclusively with the PML buffer.

3. Multi-field 2.5D FE solution

3.1. Multi-field CFS-PML decomposition

Eq. (33) provides the weak form of the CFS-PML. In the following, we introduce strain- and displacement-like auxiliary variables. Although these variables increase the number of degrees of freedom within the PML buffer with respect to a displacement-only formulation such as [36], in contrast to the conventional 2.5D PML formulation, they eliminate the need to reassemble the system matrices for each wavenumber and frequency. To this end, the stretch functions are elaborated as:

$$\lambda_s(s,\omega)=\alpha_s+\frac{\beta_s}{\omega_s+\mathrm{i}\omega}=\frac{\alpha_s\omega_s+\beta_s+\mathrm{i}\omega\alpha_s}{\omega_s+\mathrm{i}\omega}=\frac{A_s(s,\omega)}{B_s(s,\omega)}, \tag{34}$$

with attenuation parameters defined as:

$$A_s=\alpha_s\omega_s+\beta_s+\mathrm{i}\omega\alpha_s\quad\text{and}\quad B_s=\omega_s+\mathrm{i}\omega, \tag{35}$$

where the attenuation parameters A_x and B_x depend on the x-coordinate and the frequency, whereas A_z and B_z depend on the z-coordinate and the frequency. This dependency on frequency and the spatial coordinate is omitted for brevity in the following. To facilitate subsequent algebraic manipulations, B_x and B_z are expressed as:

$$B_x=\underbrace{\omega_x}_{c_0}+\underbrace{1}_{c_1}(\mathrm{i}\omega)=c_0+c_1(\mathrm{i}\omega), \tag{36}$$

$$B_z=\underbrace{\omega_z}_{d_0}+\underbrace{1}_{d_1}(\mathrm{i}\omega)=d_0+d_1(\mathrm{i}\omega). \tag{37}$$

In addition, the various cross-terms involving A_x, A_z, B_x and B_z are elaborated as:

$$A_xA_z=\underbrace{\left(\alpha_x\omega_x+\beta_x\right)\left(\alpha_z\omega_z+\beta_z\right)}_{a_0}+\underbrace{\left(\alpha_x\left(\alpha_z\omega_z+\beta_z\right)+\alpha_z\left(\alpha_x\omega_x+\beta_x\right)\right)}_{a_1}(\mathrm{i}\omega)+\underbrace{\alpha_x\alpha_z}_{a_2}(\mathrm{i}\omega)^2$$
$$=a_0+a_1(\mathrm{i}\omega)+a_2(\mathrm{i}\omega)^2, \tag{38}$$

$$B_xB_z=\underbrace{\omega_x\omega_z}_{b_0}+\underbrace{\left(\omega_x+\omega_z\right)}_{b_1}(\mathrm{i}\omega)+\underbrace{1}_{b_2}(\mathrm{i}\omega)^2=b_0+b_1(\mathrm{i}\omega)+b_2(\mathrm{i}\omega)^2, \tag{39}$$

$$A_xB_z=\underbrace{\left(\alpha_x\omega_x+\beta_x\right)\omega_z}_{\gamma_0}+\underbrace{\left(\alpha_x\left(\omega_x+\omega_z\right)+\beta_x\right)}_{\gamma_1}(\mathrm{i}\omega)+\underbrace{\alpha_x}_{\gamma_2}(\mathrm{i}\omega)^2=\gamma_0+\gamma_1(\mathrm{i}\omega)+\gamma_2(\mathrm{i}\omega)^2, \tag{40}$$

$$A_zB_x=\underbrace{\left(\alpha_z\omega_z+\beta_z\right)\omega_x}_{\delta_0}+\underbrace{\left(\alpha_z\left(\omega_x+\omega_z\right)+\beta_z\right)}_{\delta_1}(\mathrm{i}\omega)+\underbrace{\alpha_z}_{\delta_2}(\mathrm{i}\omega)^2=\delta_0+\delta_1(\mathrm{i}\omega)+\delta_2(\mathrm{i}\omega)^2, \tag{41}$$

where the parameters $a_0, a_1, a_2, b_0, b_1, b_2, c_0, c_1, d_0, d_1, \gamma_0, \gamma_1, \gamma_2, \delta_0, \delta_1$, and δ_2 depend on x and/or z, due to the spatial variability of the stretching function components ($\alpha_x, \beta_x, \omega_x$ and $\alpha_z, \beta_z, \omega_z$). Apart from this spatial variability, they remain independent of the frequency ω and the longitudinal coordinate y.

Subsequently, auxiliary strain-like fields $\hat{\boldsymbol{\xi}}$ and $\hat{\boldsymbol{\zeta}}$ are introduced, by combining terms through subtraction and addition of the terms $\lambda_z/\lambda_x\mathbf{L}_x\hat{\mathbf{u}}$ and $\lambda_x/\lambda_z\mathbf{L}_z\hat{\mathbf{u}}$, respectively:

$$\frac{\lambda_z}{\lambda_x}\mathbf{L}_x\hat{\mathbf{u}}=\mathbf{L}_{x0}\underbrace{\left(\frac{\lambda_z}{\lambda_x}-\frac{\alpha_z}{\alpha_x}\right)\frac{\partial\hat{\mathbf{u}}}{\partial x}}_{\hat{\boldsymbol{\xi}}}+\frac{\alpha_z}{\alpha_x}\mathbf{L}_x\hat{\mathbf{u}}, \tag{42}$$

$$\frac{\lambda_x}{\lambda_z}\mathbf{L}_z\hat{\mathbf{u}}=\mathbf{L}_{z0}\underbrace{\left(\frac{\lambda_x}{\lambda_z}-\frac{\alpha_x}{\alpha_z}\right)\frac{\partial\hat{\mathbf{u}}}{\partial z}}_{\hat{\boldsymbol{\zeta}}}+\frac{\alpha_x}{\alpha_z}\mathbf{L}_z\hat{\mathbf{u}}, \tag{43}$$

where the strain-like fields $\hat{\boldsymbol{\xi}}$ and $\hat{\boldsymbol{\zeta}}$ are defined as:

$$\hat{\boldsymbol{\xi}}=\left(\frac{\lambda_z}{\lambda_x}-\frac{\alpha_z}{\alpha_x}\right)\frac{\partial\hat{\mathbf{u}}}{\partial x},\quad\text{and}\quad\hat{\boldsymbol{\zeta}}=\left(\frac{\lambda_x}{\lambda_z}-\frac{\alpha_x}{\alpha_z}\right)\frac{\partial\hat{\mathbf{u}}}{\partial z}. \tag{44}$$

It is worth noting that the auxiliary variables $\hat{\boldsymbol{\xi}}$ and $\hat{\boldsymbol{\zeta}}$ comprise only three components. Nevertheless, they may be regarded as strain-like quantities, as they involve spatial derivatives of the displacement field. Furthermore, in addition to (44), a set of auxiliary displacement-like fields $\hat{\boldsymbol{\eta}}$, $\hat{\boldsymbol{\psi}}$, $\hat{\chi}$, and $\hat{\mathrm{u}}$ is introduced, defined as follows:

$$\hat{\boldsymbol{\eta}} = \left(\lambda_x\lambda_z - \alpha_x\alpha_z\right)\hat{\mathbf{u}}, \quad \hat{\boldsymbol{\psi}} = \left(\lambda_z - \alpha_z\right)\hat{\mathbf{u}}, \quad \hat{\chi} = \left(\lambda_x - \alpha_x\right)\hat{\mathbf{u}}, \quad \hat{\mathrm{u}} = \left(\frac{(\mathrm{i}\omega)^2}{B_x B_z} - 1\right)\hat{\mathbf{u}}. \tag{45}$$

The bracketed expressions in Eq. (45) may be interpreted as a filtering operator, so that the auxiliary fields $\hat{\boldsymbol{\eta}}$, $\hat{\boldsymbol{\psi}}$, $\hat{\chi}$, and $\hat{\mathrm{u}}$ can be regarded as filtered displacement variables. Making use of the relations given in (35), the term $(\mathrm{i}\omega)^2\,\lambda_x\lambda_z\hat{\mathbf{u}}$ appearing in Eq. (33) can be recast as

$$(\mathrm{i}\omega)^2\,\lambda_x\lambda_z\hat{\mathbf{u}} = A_x A_z\left(\hat{\mathbf{u}} + \hat{\mathrm{u}}\right). \tag{46}$$

Substituting Eq. (46), together with the auxiliary fields $\hat{\boldsymbol{\xi}}$, $\hat{\boldsymbol{\eta}}$, $\hat{\boldsymbol{\zeta}}$, $\hat{\boldsymbol{\psi}}$, $\hat{\chi}$, and $\hat{\mathrm{u}}$, into Eq. (33) yields:

$$\begin{aligned}
\hat{\mathbf{S}}_{\mathrm{PML}} = \int_{\Omega_{\mathrm{PML}}} \Bigg[& \frac{\alpha_z}{\alpha_x}\left(\mathbf{L}_x\hat{\mathbf{v}}\right)^{\mathrm{T}}\mathbf{C}\mathbf{L}_x + \alpha_x\alpha_z\left(\mathbf{L}_y\hat{\mathbf{v}}\right)^{\mathrm{T}}\mathbf{C}\mathbf{L}_y + \frac{\alpha_x}{\alpha_z}\left(\mathbf{L}_z\hat{\mathbf{v}}\right)^{\mathrm{T}}\mathbf{C}\mathbf{L}_z + \\
& \alpha_z\left(\left(\mathbf{L}_x\hat{\mathbf{v}}\right)^{\mathrm{T}}\mathbf{C}\mathbf{L}_y + \left(\mathbf{L}_y\hat{\mathbf{v}}\right)^{\mathrm{T}}\mathbf{C}\mathbf{L}_x\right) + \alpha_x\left(\left(\mathbf{L}_z\hat{\mathbf{v}}\right)^{\mathrm{T}}\mathbf{C}\mathbf{L}_y + \left(\mathbf{L}_y\hat{\mathbf{v}}\right)^{\mathrm{T}}\mathbf{C}\mathbf{L}_z\right) + \\
& \left(\mathbf{L}_x\hat{\mathbf{v}}\right)^{\mathrm{T}}\mathbf{C}\mathbf{L}_z + \left(\mathbf{L}_z\hat{\mathbf{v}}\right)^{\mathrm{T}}\mathbf{C}\mathbf{L}_x + \rho A_x A_z\hat{\mathbf{v}}^{\mathrm{T}}\Bigg]\hat{\mathbf{u}}\,\mathrm{d}V + \int_{\Omega_{\mathrm{PML}}}\left[\left(\mathbf{L}_x\hat{\mathbf{v}}\right)^{\mathrm{T}}\mathbf{C}\mathbf{L}_{x0}\right]\hat{\boldsymbol{\xi}}\,\mathrm{d}V + \\
& \int_{\Omega_{\mathrm{PML}}}\left[\left(\mathbf{L}_y\hat{\mathbf{v}}\right)^{\mathrm{T}}\mathbf{C}\mathbf{L}_y\right]\hat{\boldsymbol{\eta}}\,\mathrm{d}V + \int_{\Omega_{\mathrm{PML}}}\left[\left(\mathbf{L}_z\hat{\mathbf{v}}\right)^{\mathrm{T}}\mathbf{C}\mathbf{L}_{z0}\right]\hat{\boldsymbol{\zeta}}\,\mathrm{d}V + \\
& \int_{\Omega_{\mathrm{PML}}}\left[\left(\left(\mathbf{L}_x\hat{\mathbf{v}}\right)^{\mathrm{T}}\mathbf{C}\mathbf{L}_y + \left(\mathbf{L}_y\hat{\mathbf{v}}\right)^{\mathrm{T}}\mathbf{C}\mathbf{L}_x\right)\right]\hat{\boldsymbol{\psi}}\,\mathrm{d}V + \\
& \int_{\Omega_{\mathrm{PML}}}\left[\left(\left(\mathbf{L}_z\hat{\mathbf{v}}\right)^{\mathrm{T}}\mathbf{C}\mathbf{L}_y + \left(\mathbf{L}_y\hat{\mathbf{v}}\right)^{\mathrm{T}}\mathbf{C}\mathbf{L}_z\right)\right]\hat{\chi}\,\mathrm{d}V + \int_{\Omega_{\mathrm{PML}}}\rho A_x A_z\hat{\mathbf{v}}^{\mathrm{T}}\hat{\mathrm{u}}\,\mathrm{d}V.
\end{aligned} \tag{47}$$

Eq. (47), together with the weak form of definitions (44)–(45), represent the multi-field CFS-PML formulation, which is equivalent to the displacement-only CFS-PML described in Eq. (33). The weak form of definitions (44)–(45) employs the corresponding test functions $\hat{\mathbf{v}}_\xi$, $\hat{\mathbf{v}}_\eta$, $\hat{\mathbf{v}}_\zeta$, $\hat{\mathbf{v}}_\psi$, $\hat{\mathbf{v}}_\chi$ and $\hat{\mathbf{v}}_{\mathrm{u}}$, respectively:

$$\int_{\Omega_{\mathrm{PML}}} A_x B_z\hat{\mathbf{v}}_\xi^{\mathrm{T}}\hat{\boldsymbol{\xi}}\,\mathrm{d}V - \int_{\Omega_{\mathrm{PML}}}\left(A_z B_x - \frac{\alpha_z}{\alpha_x}A_x B_z\right)\hat{\mathbf{v}}_\xi^{\mathrm{T}}\frac{\partial\hat{\mathbf{u}}}{\partial x}\,\mathrm{d}V = 0, \tag{48}$$

$$\int_{\Omega_{\mathrm{PML}}} B_x B_z\hat{\mathbf{v}}_\eta^{\mathrm{T}}\hat{\boldsymbol{\eta}}\,\mathrm{d}V - \int_{\Omega_{\mathrm{PML}}}\left(A_x A_z - \alpha_x\alpha_z B_x B_z\right)\hat{\mathbf{v}}_\eta^{\mathrm{T}}\hat{\mathbf{u}}\,\mathrm{d}V = 0, \tag{49}$$

$$\int_{\Omega_{\mathrm{PML}}} A_z B_x\hat{\mathbf{v}}_\zeta^{\mathrm{T}}\hat{\boldsymbol{\zeta}}\,\mathrm{d}V - \int_{\Omega_{\mathrm{PML}}}\left(A_x B_z - \frac{\alpha_x}{\alpha_z}A_z B_x\right)\hat{\mathbf{v}}_\zeta^{\mathrm{T}}\frac{\partial\hat{\mathbf{u}}}{\partial z}\,\mathrm{d}V = 0, \tag{50}$$

$$\int_{\Omega_{\mathrm{PML}}} B_z\hat{\mathbf{v}}_\psi^{\mathrm{T}}\hat{\boldsymbol{\psi}}\,\mathrm{d}V - \int_{\Omega_{\mathrm{PML}}}\left(A_z - \alpha_z B_z\right)\hat{\mathbf{v}}_\psi^{\mathrm{T}}\hat{\mathbf{u}}\,\mathrm{d}V = 0, \tag{51}$$

$$\int_{\Omega_{\mathrm{PML}}} B_x\hat{\mathbf{v}}_\chi^{\mathrm{T}}\hat{\chi}\,\mathrm{d}V - \int_{\Omega_{\mathrm{PML}}}\left(A_x - \alpha_x B_x\right)\hat{\mathbf{v}}_\chi^{\mathrm{T}}\hat{\mathbf{u}}\,\mathrm{d}V = 0, \tag{52}$$

$$\int_{\Omega_{\mathrm{PML}}} B_x B_z\hat{\mathbf{v}}_{\mathrm{u}}^{\mathrm{T}}\hat{\mathrm{u}}\,\mathrm{d}V - \int_{\Omega_{\mathrm{PML}}}\left((\mathrm{i}\omega)^2 - B_x B_z\right)\hat{\mathbf{v}}_{\mathrm{u}}^{\mathrm{T}}\hat{\mathbf{u}}\,\mathrm{d}V = 0. \tag{53}$$

3.2. The discrete form of the 2.5D CFS-PML

Next, a 2.5D FE formulation is obtained through the introduction of the following FE discretization: As the structure is invariant along the coordinate y and has an invariant cross section A, the displacement vector $\hat{\mathbf{u}}$ and the auxiliary variables $\hat{\boldsymbol{\xi}}, \hat{\boldsymbol{\eta}}, \hat{\boldsymbol{\zeta}}, \hat{\boldsymbol{\psi}}, \hat{\chi}, \hat{\mathrm{u}}$, are discretized as:

$$\begin{aligned}
&\hat{\mathbf{u}}(\mathbf{x},\omega) \approx \mathbf{N}_{\mathrm{u}}(x,z)\underline{\hat{\mathbf{u}}}(y,\omega), \\
&\hat{\boldsymbol{\xi}}(\mathbf{x},\omega) \approx \mathbf{N}_\xi(x,z)\underline{\hat{\boldsymbol{\xi}}}(y,\omega), \quad \hat{\boldsymbol{\eta}}(\mathbf{x},\omega) \approx \mathbf{N}_\eta(x,z)\underline{\hat{\boldsymbol{\eta}}}(y,\omega), \quad \hat{\boldsymbol{\zeta}}(\mathbf{x},\omega) \approx \mathbf{N}_\zeta(x,z)\underline{\hat{\boldsymbol{\zeta}}}(y,\omega), \\
&\hat{\boldsymbol{\psi}}(\mathbf{x},\omega) \approx \mathbf{N}_\psi(x,z)\underline{\hat{\boldsymbol{\psi}}}(y,\omega), \quad \hat{\chi}(\mathbf{x},\omega) \approx \mathbf{N}_\chi(x,z)\underline{\hat{\chi}}(y,\omega), \quad \hat{\mathrm{u}}(\mathbf{x},\omega) \approx \mathbf{N}_{\mathrm{u}}(x,z)\underline{\hat{\mathrm{u}}}(y,\omega).
\end{aligned} \tag{54}$$

In the above, $\mathbf{N}_{\mathrm{u}}, \mathbf{N}_\xi, \mathbf{N}_\eta, \mathbf{N}_\zeta, \mathbf{N}_\psi, \mathbf{N}_\chi$ and $\mathbf{N}_{\mathrm{u}}$ are the globally defined shape functions defined over the section $A(x,z)$, while the vectors $\underline{\hat{\mathbf{u}}}, \underline{\hat{\boldsymbol{\xi}}}, \underline{\hat{\boldsymbol{\eta}}}, \underline{\hat{\boldsymbol{\zeta}}}, \underline{\hat{\boldsymbol{\psi}}}, \underline{\hat{\chi}}$ and $\underline{\hat{\mathrm{u}}}$ are a function of the longitudinal coordinate y and the frequency ω. The vector $\underline{\hat{\mathbf{u}}}$ contains three degrees of freedom per node on a two-dimensional mesh of cross-section A, representing a 3D wavefield in the 2.5D FE setting. The vectors $\underline{\hat{\boldsymbol{\xi}}}, \underline{\hat{\boldsymbol{\eta}}}, \underline{\hat{\boldsymbol{\zeta}}}, \underline{\hat{\boldsymbol{\psi}}}, \underline{\hat{\chi}}$, and $\underline{\hat{\mathrm{u}}}$ contain the auxiliary variables and are defined over Ω_{PML} only.

Following the standard Bubnov–Galerkin approach, identical interpolation functions (e.g., Lagrange, spectral, serendipity, ...) are employed for both trial and test functions in the multi-field CFS-PML weak forms (47)–(53). Accordingly, we define:

$$\hat{\mathbf{v}}(\mathbf{x},\omega) \approx \mathbf{N}_{\mathrm{u}}(x,z)\underline{\hat{\mathbf{v}}}_{\mathrm{u}}(y,\omega), \quad \hat{\mathbf{v}}_\square(\mathbf{x},\omega) \approx \mathbf{N}_\square(x,z)\underline{\hat{\mathbf{v}}}_\square(y,\omega), \tag{55}$$

where $\square$ denotes the auxiliary fields $\xi, \eta, \zeta, \psi, \chi$, and $\mathfrak{u}$. Substituting Eqs. (54) and (55) into Eqs. (47)–(53), and rewriting the volume integrals as integrals over the longitudinal coordinate y and the cross-sectional area A, yields:

$$
\begin{aligned}
\hat{\mathbf{S}}_{\mathrm{PML}} = &\int_{-\infty}^{\infty} \underline{\hat{\mathbf{v}}}_{\mathrm{u}}^{\mathrm{T}} \left(\int_A \frac{\alpha_z}{\alpha_x} \mathbf{B}_x^{\mathrm{T}} \mathbf{C} \mathbf{B}_x \, \mathrm{d}\Gamma \right) \underline{\hat{\mathbf{u}}} \, \mathrm{d}y + \int_{-\infty}^{\infty} \left(\frac{\partial \underline{\hat{\mathbf{v}}}_{\mathrm{u}}}{\partial y} \right)^{\mathrm{T}} \left(\int_A \alpha_x \alpha_z (\mathbf{L}_{y0} \mathbf{N}_{\mathrm{u}})^{\mathrm{T}} \mathbf{C} \mathbf{L}_{y0} \mathbf{N}_{\mathrm{u}} \, \mathrm{d}\Gamma \right) \frac{\partial \underline{\hat{\mathbf{u}}}}{\partial y} \, \mathrm{d}y \\
&+ \int_{-\infty}^{\infty} \underline{\hat{\mathbf{v}}}_{\mathrm{u}}^{\mathrm{T}} \left(\int_A \frac{\alpha_x}{\alpha_z} \mathbf{B}_z^{\mathrm{T}} \mathbf{C} \mathbf{B}_z \, \mathrm{d}\Gamma \right) \underline{\hat{\mathbf{u}}} \, \mathrm{d}y + \int_{-\infty}^{\infty} \underline{\hat{\mathbf{v}}}_{\mathrm{u}}^{\mathrm{T}} \left(\int_A \alpha_z \mathbf{B}_x^{\mathrm{T}} \mathbf{C} \mathbf{L}_{y0} \mathbf{N}_{\mathrm{u}} \, \mathrm{d}\Gamma \right) \frac{\partial \underline{\hat{\mathbf{u}}}}{\partial y} \, \mathrm{d}y \\
&+ \int_{-\infty}^{\infty} \left(\frac{\partial \underline{\hat{\mathbf{v}}}_{\mathrm{u}}}{\partial y} \right)^{\mathrm{T}} \left(\int_A \alpha_z (\mathbf{L}_{y0} \mathbf{N}_{\mathrm{u}})^{\mathrm{T}} \mathbf{C} \mathbf{B}_x \, \mathrm{d}\Gamma \right) \underline{\hat{\mathbf{u}}} \, \mathrm{d}y + \int_{-\infty}^{\infty} \underline{\hat{\mathbf{v}}}_{\mathrm{u}}^{\mathrm{T}} \left(\int_A \alpha_x \mathbf{B}_z^{\mathrm{T}} \mathbf{C} \mathbf{L}_{y0} \mathbf{N}_{\mathrm{u}} \, \mathrm{d}\Gamma \right) \frac{\partial \underline{\hat{\mathbf{u}}}}{\partial y} \, \mathrm{d}y \\
&+ \int_{-\infty}^{\infty} \left(\frac{\partial \underline{\hat{\mathbf{v}}}_{\mathrm{u}}}{\partial y} \right)^{\mathrm{T}} \left(\int_A \alpha_x (\mathbf{L}_{y0} \mathbf{N}_{\mathrm{u}})^{\mathrm{T}} \mathbf{C} \mathbf{B}_z \, \mathrm{d}\Gamma \right) \underline{\hat{\mathbf{u}}} \, \mathrm{d}y + \int_{-\infty}^{\infty} \underline{\hat{\mathbf{v}}}_{\mathrm{u}}^{\mathrm{T}} \left(\int_A \mathbf{B}_x^{\mathrm{T}} \mathbf{C} \mathbf{B}_z \, \mathrm{d}\Gamma \right) \underline{\hat{\mathbf{u}}} \, \mathrm{d}y \\
&+ \int_{-\infty}^{\infty} \underline{\hat{\mathbf{v}}}_{\mathrm{u}}^{\mathrm{T}} \left(\int_A \mathbf{B}_z^{\mathrm{T}} \mathbf{C} \mathbf{B}_x \, \mathrm{d}\Gamma \right) \underline{\hat{\mathbf{u}}} \, \mathrm{d}y + \int_{-\infty}^{\infty} \underline{\hat{\mathbf{v}}}_{\mathrm{u}}^{\mathrm{T}} \left(\int_A \rho A_x A_z \mathbf{N}_{\mathrm{u}}^{\mathrm{T}} \mathbf{N}_{\mathrm{u}} \, \mathrm{d}\Gamma \right) \underline{\hat{\mathbf{u}}} \, \mathrm{d}y \\
&+ \int_{-\infty}^{\infty} \underline{\hat{\mathbf{v}}}_{\mathrm{u}}^{\mathrm{T}} \left(\int_A \mathbf{B}_x^{\mathrm{T}} \mathbf{C} \mathbf{L}_{x0} \mathbf{N}_{\xi} \, \mathrm{d}\Gamma \right) \underline{\hat{\boldsymbol{\xi}}} \, \mathrm{d}y + \int_{-\infty}^{\infty} \left(\frac{\partial \underline{\hat{\mathbf{v}}}_{\mathrm{u}}}{\partial y} \right)^{\mathrm{T}} \left(\int_A (\mathbf{L}_{y0} \mathbf{N}_{\mathrm{u}})^{\mathrm{T}} \mathbf{C} \mathbf{L}_{y0} \mathbf{N}_{\eta} \, \mathrm{d}\Gamma \right) \frac{\partial \underline{\hat{\boldsymbol{\eta}}}}{\partial y} \, \mathrm{d}y \\
&+ \int_{-\infty}^{\infty} \underline{\hat{\mathbf{v}}}_{\mathrm{u}}^{\mathrm{T}} \left(\int_A \mathbf{B}_z^{\mathrm{T}} \mathbf{C} \mathbf{L}_{z0} \mathbf{N}_{\zeta} \, \mathrm{d}\Gamma \right) \underline{\hat{\boldsymbol{\zeta}}} \, \mathrm{d}y + \int_{-\infty}^{\infty} \underline{\hat{\mathbf{v}}}_{\mathrm{u}}^{\mathrm{T}} \left(\int_A \mathbf{B}_x^{\mathrm{T}} \mathbf{C} \mathbf{L}_{y0} \mathbf{N}_{\psi} \, \mathrm{d}\Gamma \right) \frac{\partial \underline{\hat{\boldsymbol{\psi}}}}{\partial y} \, \mathrm{d}y \\
&+ \int_{-\infty}^{\infty} \left(\frac{\partial \underline{\hat{\mathbf{v}}}_{\mathrm{u}}}{\partial y} \right)^{\mathrm{T}} \left(\int_A (\mathbf{L}_{y0} \mathbf{N}_{\mathrm{u}})^{\mathrm{T}} \mathbf{C} \mathbf{L}_x \mathbf{N}_{\psi} \, \mathrm{d}\Gamma \right) \underline{\hat{\boldsymbol{\psi}}} \, \mathrm{d}y + \int_{-\infty}^{\infty} \underline{\hat{\mathbf{v}}}_{\mathrm{u}}^{\mathrm{T}} \left(\int_A \mathbf{B}_z^{\mathrm{T}} \mathbf{C} \mathbf{L}_{y0} \mathbf{N}_{\chi} \, \mathrm{d}\Gamma \right) \frac{\partial \underline{\hat{\boldsymbol{\chi}}}}{\partial y} \, \mathrm{d}y \\
&+ \int_{-\infty}^{\infty} \left(\frac{\partial \underline{\hat{\mathbf{v}}}_{\mathrm{u}}}{\partial y} \right)^{\mathrm{T}} \left(\int_A (\mathbf{L}_{y0} \mathbf{N}_{\mathrm{u}})^{\mathrm{T}} \mathbf{C} \mathbf{L}_z \mathbf{N}_{\chi} \, \mathrm{d}\Gamma \right) \underline{\hat{\boldsymbol{\chi}}} \, \mathrm{d}y + \int_{-\infty}^{\infty} \underline{\hat{\mathbf{v}}}_{\mathrm{u}}^{\mathrm{T}} \left(\int_A \rho A_x A_z \mathbf{N}_{\mathrm{u}}^{\mathrm{T}} \mathbf{N}_{\mathfrak{u}} \, \mathrm{d}\Gamma \right) \underline{\hat{\mathfrak{u}}} \, \mathrm{d}y,
\end{aligned} \tag{56}
$$

$$
\int_{-\infty}^{\infty} \underline{\hat{\mathbf{v}}}_{\xi}^{\mathrm{T}} \left(\int_A A_x B_z \mathbf{N}_{\xi}^{\mathrm{T}} \mathbf{N}_{\xi} \, \mathrm{d}\Gamma \right) \underline{\hat{\boldsymbol{\xi}}} \, \mathrm{d}y - \int_{-\infty}^{\infty} \underline{\hat{\mathbf{v}}}_{\xi}^{\mathrm{T}} \left(\int_A \left(A_z B_x - \frac{\alpha_z}{\alpha_x} A_x B_z \right) \mathbf{N}_{\xi}^{\mathrm{T}} \mathbf{L}_{x0}^{\mathrm{T}} \mathbf{B}_x \, \mathrm{d}\Gamma \right) \underline{\hat{\mathbf{u}}} \, \mathrm{d}y = 0, \tag{57}
$$

$$
\int_{-\infty}^{\infty} \underline{\hat{\mathbf{v}}}_{\eta}^{\mathrm{T}} \left(\int_A B_x B_z \mathbf{N}_{\eta}^{\mathrm{T}} \mathbf{N}_{\eta} \, \mathrm{d}\Gamma \right) \underline{\hat{\boldsymbol{\eta}}} \, \mathrm{d}y - \int_{-\infty}^{\infty} \underline{\hat{\mathbf{v}}}_{\eta}^{\mathrm{T}} \left(\int_A \left(A_x A_z - \alpha_x \alpha_z B_x B_z \right) \mathbf{N}_{\eta}^{\mathrm{T}} \mathbf{N}_{\mathrm{u}} \, \mathrm{d}\Gamma \right) \underline{\hat{\mathbf{u}}} \, \mathrm{d}y = 0, \tag{58}
$$

$$
\int_{-\infty}^{\infty} \underline{\hat{\mathbf{v}}}_{\zeta}^{\mathrm{T}} \left(\int_A A_z B_x \mathbf{N}_{\zeta}^{\mathrm{T}} \mathbf{N}_{\zeta} \, \mathrm{d}\Gamma \right) \underline{\hat{\boldsymbol{\zeta}}} \, \mathrm{d}y - \int_{-\infty}^{\infty} \underline{\hat{\mathbf{v}}}_{\zeta}^{\mathrm{T}} \left(\int_A \left(A_x B_z - \frac{\alpha_x}{\alpha_z} A_z B_x \right) \mathbf{N}_{\zeta}^{\mathrm{T}} \mathbf{L}_{z0}^{\mathrm{T}} \mathbf{B}_z \, \mathrm{d}\Gamma \right) \underline{\hat{\mathbf{u}}} \, \mathrm{d}y = 0, \tag{59}
$$

$$
\int_{-\infty}^{\infty} \underline{\hat{\mathbf{v}}}_{\psi}^{\mathrm{T}} \left(\int_A B_z \mathbf{N}_{\psi}^{\mathrm{T}} \mathbf{N}_{\psi} \, \mathrm{d}\Gamma \right) \underline{\hat{\boldsymbol{\psi}}} \, \mathrm{d}y - \int_{-\infty}^{\infty} \underline{\hat{\mathbf{v}}}_{\psi}^{\mathrm{T}} \left(\int_A \left(A_z - \alpha_z B_z \right) \mathbf{N}_{\psi}^{\mathrm{T}} \mathbf{N}_{\mathrm{u}} \, \mathrm{d}\Gamma \right) \underline{\hat{\mathbf{u}}} \, \mathrm{d}y = 0, \tag{60}
$$

$$
\int_{-\infty}^{\infty} \underline{\hat{\mathbf{v}}}_{\chi}^{\mathrm{T}} \left(\int_A B_x \mathbf{N}_{\chi}^{\mathrm{T}} \mathbf{N}_{\chi} \, \mathrm{d}\Gamma \right) \underline{\hat{\boldsymbol{\chi}}} \, \mathrm{d}y - \int_{-\infty}^{\infty} \underline{\hat{\mathbf{v}}}_{\chi}^{\mathrm{T}} \left(\int_A \left(A_x - \alpha_x B_x \right) \mathbf{N}_{\chi}^{\mathrm{T}} \mathbf{N}_{\mathrm{u}} \, \mathrm{d}\Gamma \right) \underline{\hat{\mathbf{u}}} \, \mathrm{d}y = 0, \tag{61}
$$

$$
\int_{-\infty}^{\infty} \underline{\hat{\mathbf{v}}}_{\mathrm{u}}^{\mathrm{T}} \left(\int_A B_x B_z \mathbf{N}_{\mathrm{u}}^{\mathrm{T}} \mathbf{N}_{\mathrm{u}} \, \mathrm{d}\Gamma \right) \underline{\hat{\mathfrak{u}}} \, \mathrm{d}y - \int_{-\infty}^{\infty} \underline{\hat{\mathbf{v}}}_{\mathrm{u}}^{\mathrm{T}} \left(\int_A \left((\mathrm{i}\omega)^2 - B_x B_z \right) \mathbf{N}_{\mathrm{u}}^{\mathrm{T}} \mathbf{N}_{\mathrm{u}} \, \mathrm{d}\Gamma \right) \underline{\hat{\mathbf{u}}} \, \mathrm{d}y = 0, \tag{62}
$$

where $\mathbf{B}_x = \mathbf{L}_x \mathbf{N}_{\mathrm{u}}$ and $\mathbf{B}_z = \mathbf{L}_z \mathbf{N}_{\mathrm{u}}$ are matrices collecting the derivatives of the shape functions. Eqs. (56)–(62) are the discretized governing equations of the CFS-PML. The discretized equation is obtained through elimination of the virtual displacement vectors $\underline{\hat{\mathbf{v}}}_{\mathrm{u}}, \underline{\hat{\mathbf{v}}}_{\eta}, \underline{\hat{\mathbf{v}}}_{\psi}$ and $\underline{\hat{\mathbf{v}}}_{\chi}$. Integration by parts on the terms containing derivatives $\partial \underline{\hat{\mathbf{v}}}_{\square}(y, \omega)/\partial y$ in Eq. (56) results in:

$$
\begin{aligned}
\hat{\mathbf{S}}_{\mathrm{PML}} = &\int_{-\infty}^{\infty} \underline{\hat{\mathbf{v}}}_{\mathrm{u}}^{\mathrm{T}} \left[\int_A \frac{\alpha_z}{\alpha_x} \mathbf{B}_x^{\mathrm{T}} \mathbf{C} \mathbf{B}_x \, \mathrm{d}\Gamma + \int_A \frac{\alpha_x}{\alpha_z} \mathbf{B}_z^{\mathrm{T}} \mathbf{C} \mathbf{B}_z \, \mathrm{d}\Gamma + \int_A \mathbf{B}_x^{\mathrm{T}} \mathbf{C} \mathbf{B}_z \, \mathrm{d}\Gamma + \int_A \mathbf{B}_z^{\mathrm{T}} \mathbf{C} \mathbf{B}_x \, \mathrm{d}\Gamma \right. \\
&\left. + \int_A \rho A_x A_z \mathbf{N}_{\mathrm{u}}^{\mathrm{T}} \mathbf{N}_{\mathrm{u}} \, \mathrm{d}\Gamma \right] \underline{\hat{\mathbf{u}}} \, \mathrm{d}y + \int_{-\infty}^{\infty} \underline{\hat{\mathbf{v}}}_{\mathrm{u}}^{\mathrm{T}} \left[\int_A \mathbf{B}_x^{\mathrm{T}} \mathbf{C} \mathbf{L}_{x0} \mathbf{N}_{\xi} \, \mathrm{d}\Gamma \right] \underline{\hat{\boldsymbol{\xi}}} \, \mathrm{d}y + \int_{-\infty}^{\infty} \underline{\hat{\mathbf{v}}}_{\mathrm{u}}^{\mathrm{T}} \left[\int_A \mathbf{B}_z^{\mathrm{T}} \mathbf{C} \mathbf{L}_{z0} \mathbf{N}_{\zeta} \, \mathrm{d}\Gamma \right] \underline{\hat{\boldsymbol{\zeta}}} \, \mathrm{d}y \\
&+ \int_{-\infty}^{\infty} \underline{\hat{\mathbf{v}}}_{\mathrm{u}}^{\mathrm{T}} \left[\int_A \rho A_x A_z \mathbf{N}_{\mathrm{u}}^{\mathrm{T}} \mathbf{N}_{\mathrm{u}} \, \mathrm{d}\Gamma \right] \underline{\hat{\mathfrak{u}}} \, \mathrm{d}y + \int_{-\infty}^{\infty} \underline{\hat{\mathbf{v}}}_{\mathrm{u}}^{\mathrm{T}} \left[\int_A \alpha_z \mathbf{B}_x^{\mathrm{T}} \mathbf{C} \mathbf{L}_{y0} \mathbf{N}_{\mathrm{u}} \, \mathrm{d}\Gamma - \int_A \alpha_z (\mathbf{L}_{y0} \mathbf{N}_{\mathrm{u}})^{\mathrm{T}} \mathbf{C} \mathbf{B}_x \, \mathrm{d}\Gamma \right. \\
&\left. + \int_A \alpha_x \mathbf{B}_z^{\mathrm{T}} \mathbf{C} \mathbf{L}_{y0} \mathbf{N}_{\mathrm{u}} \, \mathrm{d}\Gamma - \int_A \alpha_x (\mathbf{L}_{y0} \mathbf{N}_{\mathrm{u}})^{\mathrm{T}} \mathbf{C} \mathbf{B}_z \, \mathrm{d}\Gamma \right] \frac{\partial \underline{\hat{\mathbf{u}}}}{\partial y} \, \mathrm{d}y + \int_{-\infty}^{\infty} \underline{\hat{\mathbf{v}}}_{\mathrm{u}}^{\mathrm{T}} \left[\int_A \mathbf{B}_x^{\mathrm{T}} \mathbf{C} \mathbf{L}_{y0} \mathbf{N}_{\psi} \, \mathrm{d}\Gamma \right. \\
&\left. - \int_A (\mathbf{L}_{y0} \mathbf{N}_{\mathrm{u}})^{\mathrm{T}} \mathbf{C} \mathbf{L}_x \mathbf{N}_{\psi} \, \mathrm{d}\Gamma \right] \frac{\partial \underline{\hat{\boldsymbol{\psi}}}}{\partial y} \, \mathrm{d}y + \int_{-\infty}^{\infty} \underline{\hat{\mathbf{v}}}_{\mathrm{u}}^{\mathrm{T}} \left[\int_A \mathbf{B}_z^{\mathrm{T}} \mathbf{C} \mathbf{L}_{y0} \mathbf{N}_{\chi} \, \mathrm{d}\Gamma - \int_A (\mathbf{L}_{y0} \mathbf{N}_{\mathrm{u}})^{\mathrm{T}} \mathbf{C} \mathbf{L}_z \mathbf{N}_{\chi} \, \mathrm{d}\Gamma \right] \frac{\partial \underline{\hat{\boldsymbol{\chi}}}}{\partial y} \, \mathrm{d}y \\
&- \int_{-\infty}^{\infty} \underline{\hat{\mathbf{v}}}_{\mathrm{u}}^{\mathrm{T}} \left[\int_A \alpha_x \alpha_z (\mathbf{L}_{y0} \mathbf{N}_{\mathrm{u}})^{\mathrm{T}} \mathbf{C} \mathbf{L}_{y0} \mathbf{N}_{\mathrm{u}} \, \mathrm{d}\Gamma \right] \frac{\partial^2 \underline{\hat{\mathbf{u}}}}{\partial y^2} \, \mathrm{d}y - \int_{-\infty}^{\infty} \underline{\hat{\mathbf{v}}}_{\mathrm{u}}^{\mathrm{T}} \left[\int_A (\mathbf{L}_{y0} \mathbf{N}_{\mathrm{u}})^{\mathrm{T}} \mathbf{C} \mathbf{L}_{y0} \mathbf{N}_{\eta} \, \mathrm{d}\Gamma \right] \frac{\partial^2 \underline{\hat{\boldsymbol{\eta}}}}{\partial y^2} \, \mathrm{d}y.
\end{aligned} \tag{63}
$$

The integrals over the cross section A in Eqs. (57)–(62) and (63) are evaluated using standard Gaussian quadrature, and solved by applying a Fourier transform of the spatial coordinate y to the wavenumber k_y, defined as $\mathcal{F}\left[f(y), k_y\right] = \int_{-\infty}^{\infty} \exp\left(+\mathrm{i} k_y y\right) f(y) \, \mathrm{d}y$, resulting in the following set of equations:

$$
\begin{aligned}
\tilde{\mathbf{S}}_{\mathrm{PML}} = &\left[\mathbf{K}_{0\mathrm{uu}} + \mathbf{K}_{1\mathrm{uu}} \left(-\mathrm{i}k_y\right) - \mathbf{K}_{2\mathrm{uu}} \left(-k_y^2\right) + \mathrm{i}\omega \mathbf{C}_{0\mathrm{uu}} - \omega^2 \mathbf{M}_{0\mathrm{uu}} \right] \underline{\tilde{\mathbf{u}}} + \mathbf{K}_{0\mathrm{u}\xi} \underline{\tilde{\boldsymbol{\xi}}} - \mathbf{K}_{2\mathrm{u}\eta} \left(-k_y^2\right) \underline{\tilde{\boldsymbol{\eta}}} \\
&+ \mathbf{K}_{0\mathrm{u}\zeta} \underline{\tilde{\boldsymbol{\zeta}}} + \mathbf{K}_{1\mathrm{u}\psi} \left(-\mathrm{i}k_y\right) \underline{\tilde{\boldsymbol{\psi}}} + \mathbf{K}_{1\mathrm{u}\chi} \left(-\mathrm{i}k_y\right) \underline{\tilde{\boldsymbol{\chi}}} + \left[\mathbf{K}_{0\mathrm{uu}} + \mathrm{i}\omega \mathbf{C}_{0\mathrm{uu}} - \omega^2 \mathbf{M}_{0\mathrm{uu}} \right] \underline{\tilde{\mathfrak{u}}}
\end{aligned} \tag{64}
$$

$$\left[\mathbf{K}_{0\xi\xi} + \mathrm{i}\omega\mathbf{C}_{0\xi\xi} - \omega^2\mathbf{M}_{0\xi\xi}\right]\underline{\tilde{\boldsymbol{\xi}}} - \left[\mathbf{K}_{0\xi u} + \mathrm{i}\omega\mathbf{C}_{0\xi u} - \omega^2\mathbf{M}_{0\xi u}\right]\underline{\tilde{\mathbf{u}}} = 0, \tag{65}$$

$$\left[\mathbf{K}_{0\eta\eta} + \mathrm{i}\omega\mathbf{C}_{0\eta\eta} - \omega^2\mathbf{M}_{0\eta\eta}\right]\underline{\tilde{\boldsymbol{\eta}}} - \left[\mathbf{K}_{0\eta u} + \mathrm{i}\omega\mathbf{C}_{0\eta u} - \omega^2\mathbf{M}_{0\eta u}\right]\underline{\tilde{\mathbf{u}}} = 0, \tag{66}$$

$$\left[\mathbf{K}_{0\zeta\zeta} + \mathrm{i}\omega\mathbf{C}_{0\zeta\zeta} - \omega^2\mathbf{M}_{0\zeta\zeta}\right]\underline{\tilde{\boldsymbol{\zeta}}} - \left[\mathbf{K}_{0\zeta u} + \mathrm{i}\omega\mathbf{C}_{0\zeta u} - \omega^2\mathbf{M}_{0\zeta u}\right]\underline{\tilde{\mathbf{u}}} = 0, \tag{67}$$

$$\left[\mathbf{K}_{0\psi\psi} + \mathrm{i}\omega\mathbf{C}_{0\psi\psi}\right]\underline{\tilde{\boldsymbol{\psi}}} - \mathbf{K}_{0\psi u}\underline{\tilde{\mathbf{u}}} = 0, \tag{68}$$

$$\left[\mathbf{K}_{0\chi\chi} + \mathrm{i}\omega\mathbf{C}_{0\chi\chi}\right]\underline{\tilde{\chi}} - \mathbf{K}_{0\chi u}\underline{\tilde{\mathbf{u}}} = 0, \tag{69}$$

$$\left[\mathbf{K}_{0uu} + \mathrm{i}\omega\mathbf{C}_{0uu} - \omega^2\mathbf{M}_{0uu}\right]\underline{\tilde{\mathbf{u}}} - \left[\mathbf{K}_{0u_u} + \mathrm{i}\omega\mathbf{C}_{0u_u} - \omega^2\mathbf{M}_{0u_u}\right]\underline{\tilde{\mathbf{u}}} = 0. \tag{70}$$

A tilde above a variable indicates its representation in the wavenumber–frequency domain. The stiffness, damping, and mass matrices appearing in Eqs. (64)–(70) are listed in Appendix. Using the coefficient definitions provided in (36)–(41) for the CFS-PML formulation [44], it follows that the frequency ω enters Eqs. (64)–(70) at most quadratically.

By reintroducing the 2.5D dynamic stiffness matrices, corresponding to the displacement-based formulation for the interior domain Ω_{ID} in Eq. (30), and the mixed formulation of the PML buffer Ω_{PML} (in Eqs. (64)–(70)), into Eq. (29), we obtain the governing equation for the entire computational domain $\Omega_{\mathrm{ID}} \cup \Omega_{\mathrm{PML}}$:

$$\left(\mathbf{K}_0 - \mathrm{i}k_y\mathbf{K}_1 - k_y^2\mathbf{K}_2 + \mathrm{i}\omega\mathbf{C}_0 - \omega^2\mathbf{M}_0\right)\underline{\tilde{\mathbf{d}}} = \underline{\tilde{\mathbf{p}}}, \tag{71}$$

where the stiffness matrices $\mathbf{K}_0, \mathbf{K}_1, \mathbf{K}_2$, damping matrix $\mathbf{C}_0$, and mass matrix $\mathbf{M}_0$ are defined as:

$$\begin{aligned} &\mathbf{K}_0 = \mathbf{K}_{0,\mathrm{ID}} + \mathbf{K}_{0,\mathrm{PML}}, \quad \mathbf{K}_1 = \mathbf{K}_{1,\mathrm{ID}} + \mathbf{K}_{1,\mathrm{PML}}, \quad \mathbf{K}_2 = \mathbf{K}_{2,\mathrm{ID}} + \mathbf{K}_{2,\mathrm{PML}}, \\ &\mathbf{C}_0 = \mathbf{C}_{0,\mathrm{PML}}, \quad \mathbf{M}_0 = \mathbf{M}_{0,\mathrm{ID}} + \mathbf{M}_{0,\mathrm{PML}}. \end{aligned} \tag{72}$$

These system matrices are frequency-independent, as intended, where the resulting system of equations takes the same form as the classical 2.5D case [20]. The contributions $\mathbf{K}_{0,\mathrm{ID}}, \mathbf{K}_{1,\mathrm{ID}}, \mathbf{K}_{2,\mathrm{ID}}$, and $\mathbf{M}_{0,\mathrm{ID}}$ to the global stiffness and mass matrices, respectively, are the standard 2.5D stiffness and consistent mass matrices of a displacement-based FE method for the interior domain Ω_{ID} [20]. The stiffness matrices $\mathbf{K}_{0,\mathrm{PML}}, \mathbf{K}_{1,\mathrm{PML}}$ and $\mathbf{K}_{2,\mathrm{PML}}$ for the PML domain Ω_{PML} are defined as:

$$\mathbf{K}_{0,\mathrm{PML}} = \begin{bmatrix} \mathbf{K}_{0uu} & \mathbf{K}_{0u\xi} & \mathbf{0} & \mathbf{K}_{0u\zeta} & \mathbf{0} & \mathbf{0} & \mathbf{K}_{0uu} \\ -\mathbf{K}_{0\xi u} & \mathbf{K}_{0\xi\xi} & \mathbf{0} & \mathbf{0} & \mathbf{0} & \mathbf{0} & \mathbf{0} \\ -\mathbf{K}_{0\eta u} & \mathbf{0} & \mathbf{K}_{0\eta\eta} & \mathbf{0} & \mathbf{0} & \mathbf{0} & \mathbf{0} \\ -\mathbf{K}_{0\zeta u} & \mathbf{0} & \mathbf{0} & \mathbf{K}_{0\zeta\zeta} & \mathbf{0} & \mathbf{0} & \mathbf{0} \\ -\mathbf{K}_{0\psi u} & \mathbf{0} & \mathbf{0} & \mathbf{0} & \mathbf{K}_{0\psi\psi} & \mathbf{0} & \mathbf{0} \\ -\mathbf{K}_{0\chi u} & \mathbf{0} & \mathbf{0} & \mathbf{0} & \mathbf{0} & \mathbf{K}_{0\chi\chi} & \mathbf{0} \\ -\mathbf{K}_{0u_u} & \mathbf{0} & \mathbf{0} & \mathbf{0} & \mathbf{0} & \mathbf{0} & \mathbf{K}_{0uu} \end{bmatrix} \tag{73}$$

$$\mathbf{K}_{1,\mathrm{PML}} = \begin{bmatrix} \mathbf{K}_{1uu} & \mathbf{0} & \mathbf{0} & \mathbf{0} & \mathbf{K}_{1u\psi} & \mathbf{K}_{1u\chi} & \mathbf{0} \\ \mathbf{0} & \mathbf{0} & \mathbf{0} & \mathbf{0} & \mathbf{0} & \mathbf{0} & \mathbf{0} \\ \mathbf{0} & \mathbf{0} & \mathbf{0} & \mathbf{0} & \mathbf{0} & \mathbf{0} & \mathbf{0} \\ \mathbf{0} & \mathbf{0} & \mathbf{0} & \mathbf{0} & \mathbf{0} & \mathbf{0} & \mathbf{0} \\ \mathbf{0} & \mathbf{0} & \mathbf{0} & \mathbf{0} & \mathbf{0} & \mathbf{0} & \mathbf{0} \\ \mathbf{0} & \mathbf{0} & \mathbf{0} & \mathbf{0} & \mathbf{0} & \mathbf{0} & \mathbf{0} \\ \mathbf{0} & \mathbf{0} & \mathbf{0} & \mathbf{0} & \mathbf{0} & \mathbf{0} & \mathbf{0} \end{bmatrix}, \tag{74}$$

and

$$\mathbf{K}_{2,\mathrm{PML}} = \begin{bmatrix} -\mathbf{K}_{2uu} & \mathbf{0} & -\mathbf{K}_{2u\eta} & \mathbf{0} & \mathbf{0} & \mathbf{0} & \mathbf{0} \\ \mathbf{0} & \mathbf{0} & \mathbf{0} & \mathbf{0} & \mathbf{0} & \mathbf{0} & \mathbf{0} \\ \mathbf{0} & \mathbf{0} & \mathbf{0} & \mathbf{0} & \mathbf{0} & \mathbf{0} & \mathbf{0} \\ \mathbf{0} & \mathbf{0} & \mathbf{0} & \mathbf{0} & \mathbf{0} & \mathbf{0} & \mathbf{0} \\ \mathbf{0} & \mathbf{0} & \mathbf{0} & \mathbf{0} & \mathbf{0} & \mathbf{0} & \mathbf{0} \\ \mathbf{0} & \mathbf{0} & \mathbf{0} & \mathbf{0} & \mathbf{0} & \mathbf{0} & \mathbf{0} \\ \mathbf{0} & \mathbf{0} & \mathbf{0} & \mathbf{0} & \mathbf{0} & \mathbf{0} & \mathbf{0} \end{bmatrix} \tag{75}$$

The damping matrix $\mathbf{C}_{0,\mathrm{PML}}$ is:

$$\mathbf{C}_{0,\mathrm{PML}} = \begin{bmatrix} \mathbf{C}_{0uu} & \mathbf{0} & \mathbf{0} & \mathbf{0} & \mathbf{0} & \mathbf{0} & \mathbf{C}_{0uu} \\ -\mathbf{C}_{0\xi u} & \mathbf{C}_{0\xi\xi} & \mathbf{0} & \mathbf{0} & \mathbf{0} & \mathbf{0} & \mathbf{0} \\ -\mathbf{C}_{0\eta u} & \mathbf{0} & \mathbf{C}_{0\eta\eta} & \mathbf{0} & \mathbf{0} & \mathbf{0} & \mathbf{0} \\ -\mathbf{C}_{0\zeta u} & \mathbf{0} & \mathbf{0} & \mathbf{C}_{0\zeta\zeta} & \mathbf{0} & \mathbf{0} & \mathbf{0} \\ \mathbf{0} & \mathbf{0} & \mathbf{0} & \mathbf{0} & \mathbf{C}_{0\psi\psi} & \mathbf{0} & \mathbf{0} \\ \mathbf{0} & \mathbf{0} & \mathbf{0} & \mathbf{0} & \mathbf{0} & \mathbf{C}_{0\chi\chi} & \mathbf{0} \\ -\mathbf{C}_{0u_u} & \mathbf{0} & \mathbf{0} & \mathbf{0} & \mathbf{0} & \mathbf{0} & \mathbf{C}_{0uu} \end{bmatrix}, \tag{76}$$

and the mass matrix $\mathbf{M}_{0,\mathrm{PML}}$ is defined as:

$$\mathbf{M}_{0,\mathrm{PML}} = \begin{bmatrix} \mathbf{M}_{0uu} & \mathbf{0} & \mathbf{0} & \mathbf{0} & \mathbf{0} & \mathbf{0} & \mathbf{M}_{0uu} \\ -\mathbf{M}_{0\xi u} & \mathbf{M}_{0\xi\xi} & \mathbf{0} & \mathbf{0} & \mathbf{0} & \mathbf{0} & \mathbf{0} \\ -\mathbf{M}_{0\eta u} & \mathbf{0} & \mathbf{M}_{0\eta\eta} & \mathbf{0} & \mathbf{0} & \mathbf{0} & \mathbf{0} \\ -\mathbf{M}_{0\zeta u} & \mathbf{0} & \mathbf{0} & \mathbf{M}_{0\zeta\zeta} & \mathbf{0} & \mathbf{0} & \mathbf{0} \\ \mathbf{0} & \mathbf{0} & \mathbf{0} & \mathbf{0} & \mathbf{0} & \mathbf{0} & \mathbf{0} \\ \mathbf{0} & \mathbf{0} & \mathbf{0} & \mathbf{0} & \mathbf{0} & \mathbf{0} & \mathbf{0} \\ -\mathbf{M}_{0uu} & \mathbf{0} & \mathbf{0} & \mathbf{0} & \mathbf{0} & \mathbf{0} & \mathbf{M}_{0uu} \end{bmatrix}. \tag{77}$$

In Eq. (71), the vector of nodal unknowns $\underline{\tilde{\mathbf{d}}}$ includes displacements, auxiliary strain fields, and the filtered displacements, i.e.:

$$\underline{\tilde{\mathbf{d}}} = \left\{ \underline{\tilde{\mathbf{u}}},\ \underline{\tilde{\xi}},\ \underline{\tilde{\eta}},\ \underline{\tilde{\zeta}},\ \underline{\tilde{\psi}},\ \underline{\tilde{\chi}},\ \underline{\tilde{\mathrm{u}}} \right\}^{\mathrm{T}}. \tag{78}$$

We note that the nodal displacement vector $\underline{\hat{\mathbf{u}}}$ is defined over the entire domain $\Omega_{\mathrm{ID}} \cup \Omega_{\mathrm{PML}}$, whereas the nodal auxiliary degrees of freedom $\underline{\hat{\xi}}$, $\underline{\hat{\eta}}$, $\underline{\hat{\zeta}}$, $\underline{\hat{\psi}}$, $\underline{\hat{\chi}}$ and $\underline{\hat{\mathrm{u}}}$ are defined over the PML domain Ω_{PML} only. Similarly, the load vector $\underline{\tilde{\mathbf{p}}} = \left\{ \int_{\Gamma_{\mathrm{ID}}^{\mathrm{L}}} \mathbf{N}_{\mathrm{u}}^{\mathrm{T}} \underline{\tilde{\mathbf{p}}}_{0,\mathrm{ID}} \, \mathrm{d}A, \mathbf{0}, \mathbf{0}, \mathbf{0}, \mathbf{0}, \mathbf{0}, \mathbf{0} \right\}^{\mathrm{T}}$ corresponds to the loading vector along the boundary $\Gamma_{\mathrm{ID}}^{\mathrm{L}}$ of the interior domain. Eq. (71) is solved for a range of wavenumbers and frequencies. Inverse Fourier transforms of the wavenumber k_y to the spatial coordinate y and of the frequency ω to the time t subsequently yield the solution in the space–time domain.

In the case where the frequency shifts ω_x and ω_z are set to zero, the formulation reduces to a standard 2.5D PML formulation. Furthermore, setting the spatial stretches λ_x and λ_z to unity further simplifies it to the standard elastodynamic case.

3.3. Numerical implementation and element technology

In view of the choice of shape functions and element types for the CFS-PML implementation, it is instructive to investigate the continuity requirements on the displacement field and the various auxiliary fields.

As in standard plane elasticity, the displacement field requires C^0 continuity because its approximation appears through derivatives of the shape functions (i.e., the terms $\mathbf{B}_x = \mathbf{L}_x\mathbf{N}_{\mathrm{u}}$ and $\mathbf{B}_z = \mathbf{L}_z\mathbf{N}_{\mathrm{u}}$). Consequently, conventional C^0 continuous finite element shape functions are suitable for the displacement interpolation.

In contrast, the discretized governing equations of the CFS-PML formulation (Eqs. (56)–(62)) do not involve derivatives of the auxiliary fields $\tilde{\xi}$, $\tilde{\eta}$, $\tilde{\zeta}$, and $\tilde{\mathrm{u}}$. Therefore, only C^{-1} continuity is required for the corresponding shape functions $\mathbf{N}_\xi$, $\mathbf{N}_\eta$, $\mathbf{N}_\zeta$, and $\mathbf{N}_{\mathrm{u}}$, i.e. the shape functions can be discontinuous across element boundaries but should be integrable.

An exception arises for the auxiliary fields $\tilde{\psi}$ and $\tilde{\chi}$, whose derivatives $\mathbf{L}_x\mathbf{N}_\psi$ and $\mathbf{L}_z\mathbf{N}_\chi$ appear explicitly in Eq. (56). As a result, their shape functions $\mathbf{N}_\psi$ and $\mathbf{N}_\chi$ must satisfy a C^0-continuity requirement, analogous to the displacement interpolation.

The C^{-1} continuity requirement for $\tilde{\xi}$, $\tilde{\eta}$, $\tilde{\zeta}$, and $\tilde{\mathrm{u}}$ provides flexibility in choosing their interpolation. One strategy is to approximate these fields using constant shape functions per element. Applied to the standard 4-node bilinear quadrilateral (Q4), 8-node quadratic serendipity quadrilateral (Q8), and 6-node quadratic triangular (T6) elements, this yields the Q41, Q81, and T61 elements, respectively, as shown in Fig. 3. Each element includes a single interior node assigned to the auxiliary unknowns. This choice minimizes the number of additional degrees of freedom introduced by the PML formulation and thereby reduces computational cost.

Alternatively, the auxiliary fields may be interpolated using the same shape functions as the displacement field. This results in the Q44, Q88, and T66 elements as shown in Fig. 3, wherein displacement and auxiliary variables share the same polynomial order. Although this approach increases the number of auxiliary degrees of freedom, it ensures a uniform interpolation space across all fields and is therefore expected to improve solution accuracy.

In all subsequent numerical simulations, Gauss–Legendre quadrature rules are selected to ensure accurate numerical integration of the element matrices. For the bilinear quadrilateral elements (Q41 and Q44), a standard 2×2 Gauss quadrature scheme is employed, which exactly integrates the polynomial terms associated with these elements. For the higher-order quadrilateral elements (Q81 and Q88), a 3×3 Gaussian integration scheme is used. The triangular elements (T61 and T66) are integrated using a 4-point triangular Gauss–Legendre quadrature scheme.

4. Numerical examples

This section presents numerical examples that are arranged in order of increasing complexity and intends to demonstrate complementary aspects of the proposed 2.5D CFS-PML formulation. First, the one-dimensional (1D) wave propagation in a semi-infinite bar is considered. This benchmark example provides verification of the numerical implementation and insight into the effect of the CFS-PML parameters on propagating waves impinging at normal incidence. Next, the solution to 2D wave propagation in a homogeneous halfspace is computed and compared with a reference solution to assess the absorbing performance of the CFS-PML in the frequency–wavenumber domain. This example specifically investigates the behavior of the formulation for propagating and evanescent waves over a wide range of longitudinal wavenumbers, including waves propagating at grazing incidence to the PML interface, and for which the complex frequency shift is expected to provide improved absorption. This example is then extended to a laterally truncated, shallow 3D domain, in which guided-wave energy traveling close to the free surface impinges on the PML at near-grazing incidence. Subsequently, the dynamic soil–structure interaction between a cut-and-cover tunnel and the surrounding

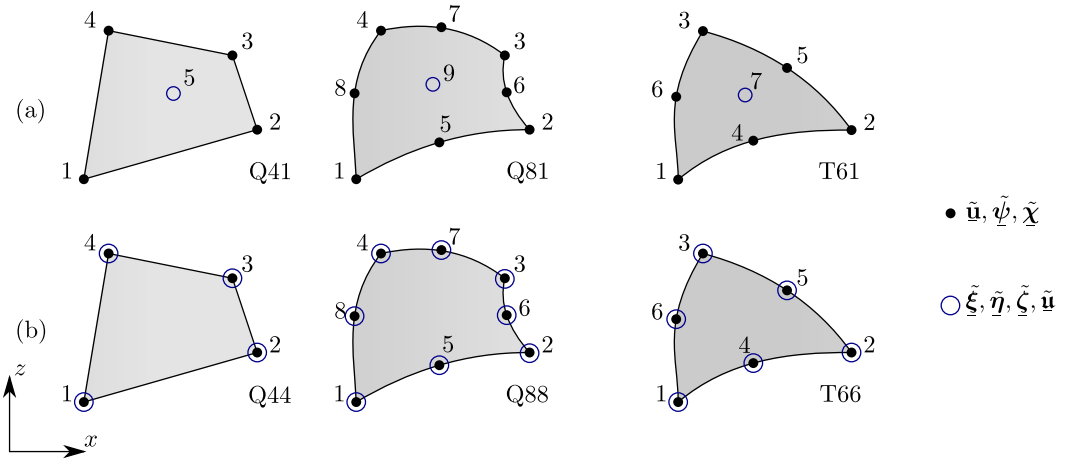

Fig. 3. Overview of the 2.5D CFS-PML finite elements implemented: (a) Q41, Q81, and T61 elements with a central node for the interpolation of the auxiliary fields, and (b) Q44, Q88, and T66 elements using the same shape functions for interpolation of the displacement and auxiliary fields.

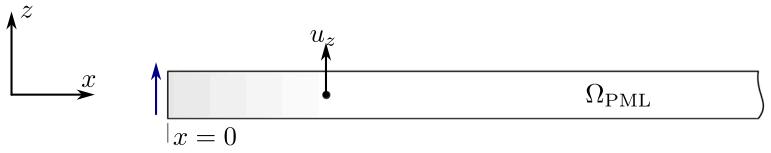

Fig. 4. 1D bar under shear loading.

soil is computed as an application of the proposed method in a 2.5D setting. This final example demonstrates the applicability of the formulation to a realistic engineering problem and highlights the computational benefits associated with frequency- and wavenumber-independent system matrices.

4.1. One-dimensional wave propagation in a semi-infinite bar

The effect of the parameterization of the CFS-PML on its behavior is studied by means of the analytical solution of 1D (shear) wave propagation in a semi-infinite bar (Fig. 4), $0 \leq x \leq \infty$, under imposed unit transverse harmonic displacement at $x = 0$. The bar consists of a stretched medium, considering the general form of the CFS-PML stretch function, as per Eq. (5). This simplified 1D example enables a first assessment of the CFS-PML behavior for waves impinging at normal incidence on the absorbing layer, and clarifies the effects of PML truncation and FE discretization. This 1D problem, however, does not capture phenomena associated with oblique incidence, for which the effectiveness of the PML may differ. Numerical examples aimed at straining the PML more severely than normal incidence does are reported later in this section.

For the 1D problem at hand, the stretch function defined in Eq. (5), together with the spatial dependence of the parameters $\alpha_x(x)$ (Eq. (7)), $\beta_x(x)$ (Eq. (8)), and $\omega_x(x)$ (Eq. (9)), is explicitly integrated in the mapping (1), yielding the stretched coordinate $\tilde{x}$:

$$\tilde{x} = x + \left(\alpha_0 + \frac{\beta_0 \omega_0}{\omega_0^2 + \omega^2} - \mathrm{i} \frac{\beta_0 \omega}{\omega_0^2 + \omega^2} \right) \frac{x^{m_0+1}}{L_{\mathrm{PML}}^{m_0} \left(m_0 + 1\right)}. \tag{79}$$

The wave propagation solution in the bar is then obtained by substituting the physical coordinate x with its stretched counterpart $\tilde{x}$ in a plane wave solution, resulting in:

$$\hat{u}(x) = \exp\left(-\mathrm{i} k_{\mathrm{s}} \tilde{x}\right). \tag{80}$$

Using Eq. (79), the displacement solution is elaborated as the product of three exponential factors:

$$\hat{u}(x) = \underbrace{\exp\left(-\mathrm{i}\, k_{\mathrm{s}}\, x\right)}_{\text{(I)}} \underbrace{\exp\left(-\mathrm{i}\, k_{\mathrm{s}} \left(\alpha_0 + \frac{\beta_0\, \omega_0}{\omega_0^2 + \omega^2} \right) \frac{x^{m_0+1}}{L_{\mathrm{PML}}^{m_0}(m_0+1)} \right)}_{\text{(II)}} \underbrace{\exp\left(- k_{\mathrm{s}} \frac{\beta_0\, \omega}{\omega_0^2 + \omega^2} \frac{x^{m_0+1}}{L_{\mathrm{PML}}^{m_0}(m_0+1)} \right)}_{\text{(III)}}. \tag{81}$$

The first factor (I) represents the unattenuated plane wave propagating in a 1D elastic bar with wavenumber k_{s}. The second factor (II) has an imaginary exponent and therefore modulates the phase of the solution. It can be interpreted as an artificial (physical)

stretching of the coordinate inside the PML. The third factor (III) has a strictly real and negative exponent that enforces exponential decay of the amplitude as x increases in the PML buffer, where the decay rate is controlled by the parameter β_0 and the frequency ω relative to the shift ω_0. The phase-modulating term (II) and the exponentially decaying term (III) ensure that waves are sufficiently damped before reaching the truncation boundary.

Parameterization of the standard PML

For a standard PML, setting $\omega_0 = 0$ allows Eq. (81) to be elaborated as

$$\hat{u}(x) = \underbrace{\exp\left(-\mathrm{i}\, k_s\, x\right)}_{\text{(I)}} \underbrace{\exp\left(-\mathrm{i}\, k_s\, \alpha_0\, \frac{x^{m_0+1}}{L_{\text{PML}}^{m_0}(m_0+1)} \right)}_{\text{(II)}} \underbrace{\exp\left(-k_s\, \frac{\beta_0}{\omega}\, \frac{x^{m_0+1}}{L_{\text{PML}}^{m_0}(m_0+1)} \right)}_{\text{(III)}}. \tag{82}$$

Eq. (82) shows that the parameter α_0 controls the physical stretching in term (II). When the PML is discretized numerically, an adequate number of elements per (apparent) wavelength is required to accurately resolve the displacement field. Increasing α_0 introduces artificial stretching, which reduces the apparent wavelength and necessitates a finer mesh; a similar effect can be achieved by enlarging the PML domain. Therefore, it is common practice to set $\alpha_0 = 0$ (i.e., $\alpha_x = 1$), corresponding to no physical stretch. In this case, absorption within the PML is controlled by increasing its length L_{PML} and selecting element sizes according to standard guidelines, e.g., the number of elements per wavelength.

With the specific choice $\alpha_0 = 0$, solution (82) simplifies to

$$\hat{u}(x) = \exp\left(-\mathrm{i}\, k_s\, x\right) \exp\left(-k_s\, \frac{\beta_0}{\omega}\, \frac{x^{m_0+1}}{L_{\text{PML}}^{m_0}(m_0+1)} \right). \tag{83}$$

For a fixed PML length L_{PML}, the parameter β_0 can be chosen to achieve a prescribed attenuation in the solution (83). By fixing the exponent of the attenuation term at $x = L_{\text{PML}}$ to

$$a = \frac{1}{C_s}\, \beta_0\, \frac{L_{\text{PML}}}{m_0+1}, \tag{84}$$

β_0 is computed as

$$\beta_0 = a\, \frac{C_s}{L_{\text{PML}}}\, (m_0+1). \tag{85}$$

A typical choice for the attenuation parameter is $a = 10$, corresponding to $\exp(-10) \approx 4.54 \times 10^{-5}$ [53], which provides a balance between sufficient damping of propagating waves and minimizing numerical reflections. Under these conditions (i.e., $\omega_0 = 0$, $\alpha_0 = 0$, and β_0 obtained from Eq. (85)), the solution of the wave Eq. (81) for the standard PML becomes

$$\hat{u}(x) = \exp\left(-\mathrm{i}\, k_s\, x\right) \exp\left(-a \left(\frac{x}{L_{\text{PML}}} \right)^{m_0+1} \right). \tag{86}$$

Since the second factor depends only on the spatial coordinate x, this formulation demonstrates that, regardless of frequency, any propagating wave is attenuated uniformly within the PML.

Parameterization of the CFS-PML

For the CFS-PML, we consider the same choice for the parameters α_0 and β_0 as for the standard PML, i.e. $\alpha_0 = 0$ and β_0 obtained from Eq. (85), and study the effect of the frequency shift ω_0. With this particular choice, the 1D wave propagation solution in Eq. (81) is elaborated as:

$$\hat{u}(x) = \exp\left(-\mathrm{i} k_s x\right) \exp\left(-\mathrm{i} a\, \underbrace{\frac{\omega_0 \omega}{\omega_0^2+\omega^2}}_{\hat{\Lambda}(\omega)} \left(\frac{x}{L_{\text{PML}}} \right)^{m_0+1} \right) \exp\left(-a\, \underbrace{\frac{\omega^2}{\omega_0^2+\omega^2}}_{\hat{\Gamma}(\omega)} \left(\frac{x}{L_{\text{PML}}} \right)^{m_0+1} \right). \tag{87}$$

Hence, the frequency shift ω_0 results in a frequency-dependent artificial stretch and wave attenuation, given by the factors

$$\hat{\Lambda}(\omega) = \frac{\frac{\omega}{\omega_0}}{1 + \left(\frac{\omega}{\omega_0} \right)^2}, \tag{88}$$

and

$$\hat{\Gamma}(\omega) = \frac{\left(\frac{\omega}{\omega_0} \right)^2}{1 + \left(\frac{\omega}{\omega_0} \right)^2}, \tag{89}$$

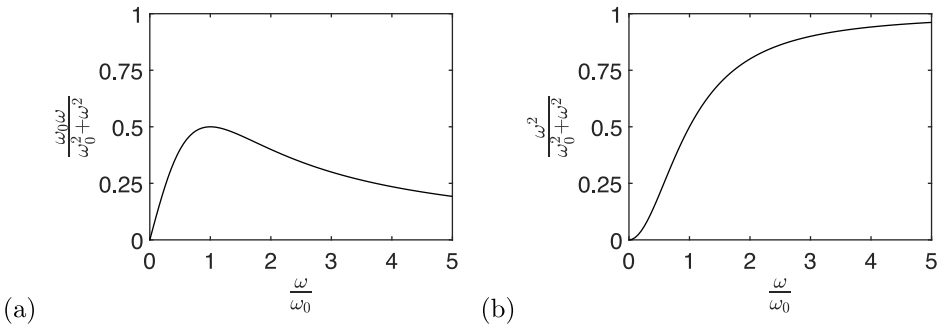

Fig. 5. The factors (a) $\hat{\Lambda}(\omega)$ and (b) $\hat{\Gamma}(\omega)$ as a function of the dimensionless frequency ω/ω_0.

Fig. 6. FE meshes for the 1D bar problem for (a) the quadrilateral Q41, Q44, Q81, and Q88 elements and (b) the triangular T61 and T66 elements.

plotted in Fig. 5 as a function of the dimensionless frequency ω/ω_0. The factor $\hat{\Lambda}(\omega)$ attains a maximum value of 0.5 at $\omega = \omega_0$, and converges to zero as ω approaches infinity. The factor $\hat{\Gamma}(\omega)$ increases monotonically to a value of 1 at limiting high frequencies, reaching a value of 0.5 at $\omega = \omega_0$. As a result, the frequency shift ω_0 reduces the attenuation of propagating waves at low frequencies, while an artificial stretch is provided with a maximum at the frequency shift ω_0.

It should be noted that the 1D problem considered here does not allow us to fully explore the advantages of the frequency shift ω_0, as the 1D solution consists only of propagating waves at normal incidence. The factor $\hat{\Lambda}(\omega)$ improves the accuracy of the solution of evanescent waves around $\omega = \omega_0$, while still providing sufficient attenuation of propagating waves through the factor $\hat{\Gamma}(\omega)$. At high frequencies, the CFS-PML approaches the attenuation of the standard PML.

Numerical solution

The CFS-PML formulation is numerically evaluated for shear wave propagation in a one-dimensional bar as an initial verification of the implementation. In order to analyze the reflective properties of the PML, the first half of the bar ($0 < x < L_{\text{PML}}$) is considered to be an undamped linear elastic, whereas the second half of the bar ($L_{\text{PML}} < x < L_{\text{tot}} = 2L_{\text{PML}}$) is damped with CFS-PML parameters.

Numerical results are obtained using the Q41, Q81, T61, Q44, Q88, and T66 finite elements. The model consists of a bar of length $L_{\text{tot}} = 100\,\text{m}$, characterized by a shear wave velocity $C_s = 150\,\text{m/s}$ and a density $\rho = 1800\,\text{kg/m}^3$. The PML parameters are chosen as $\alpha_0 = 0$ and β_0 obtained from Eq. (85) ($a = 10$). Frequency shifts ($f_0 = \omega_0/(2\pi) = 0\,\text{Hz}$) and $f_0 = 10\,\text{Hz}$ are considered, corresponding to a classical PML stretch function and a CFS-PML stretch function.

A unit transverse harmonic displacement at a frequency of 10 Hz is applied at $x = 0$, and only vertical degrees of freedom are retained, thereby generating shear waves along the bar. The boundary at $x = L_{\text{tot}}$ is clamped. A uniform mesh with element size $l_{\text{el}} = 2\,\text{m}$ is employed, resulting in 50 quadrilateral elements and 100 triangular elements, as illustrated in Fig. 6, resulting in 7.5 elements per wavelength ($\lambda_s = 15\,\text{m}$) at the frequency of 10 Hz.

As the response is limited to one-dimensional wave propagation, the wavenumber k_y is set to 0, so that the system (71) reduces to:

$$\left(\mathbf{K}_0 + \mathrm{i}\omega\mathbf{C}_0 - \omega^2\mathbf{M}_0\right)\underline{\tilde{\mathbf{d}}} = \underline{\tilde{\mathbf{p}}}, \tag{90}$$

and only the matrices $\mathbf{K}_0$, $\mathbf{C}_0$, and $\mathbf{M}_0$ are effectively used.

Fig. 7 compares the displacement obtained with the different CFS-PML finite elements with the analytical solution for the CFS-PML without and with a frequency shift ($f_0 = \omega_0/(2\pi) = 0\,\text{Hz}$ and $f_0 = 10\,\text{Hz}$). The real and imaginary components of the vertical displacement are shown along the normalized bar length $\xi = x/L_{\text{PML}}$. Correspondingly, a propagating wave solution is expected between $0 < \xi < 1$, whereas between $1 < \xi < 2$, the solution reduces to (81).

All element types correctly reproduce the attenuating wavefield in the PML, although differences arise depending on the interpolation of the auxiliary fields. The elements that use the same interpolation for displacement and auxiliary variables (Q44, Q88, T66) generally show improved accuracy, particularly for a frequency shift of $f_0 = 10\,\text{Hz}$. In contrast, the elements with reduced-order auxiliary interpolation (Q41, Q81, T61) may exhibit small deviations from the reference solution. For an increasing number of elements, the numerical solution converges to the analytical solution for all element types. Overall, the results validate the numerical implementation of the CFS-PML and highlight the influence of the interpolation order on accuracy. Furthermore, the accuracy of the displacement field within the PML ($1 < \xi < 2$) is of limited practical importance, as long as the absorptive performance of the PML is attained. Consistent with this observation, a related investigation [44] comparing the 2D Q41 and Q81 elements with their Q44 and Q88 counterparts reports that the overall attenuation characteristics remain effectively equivalent.

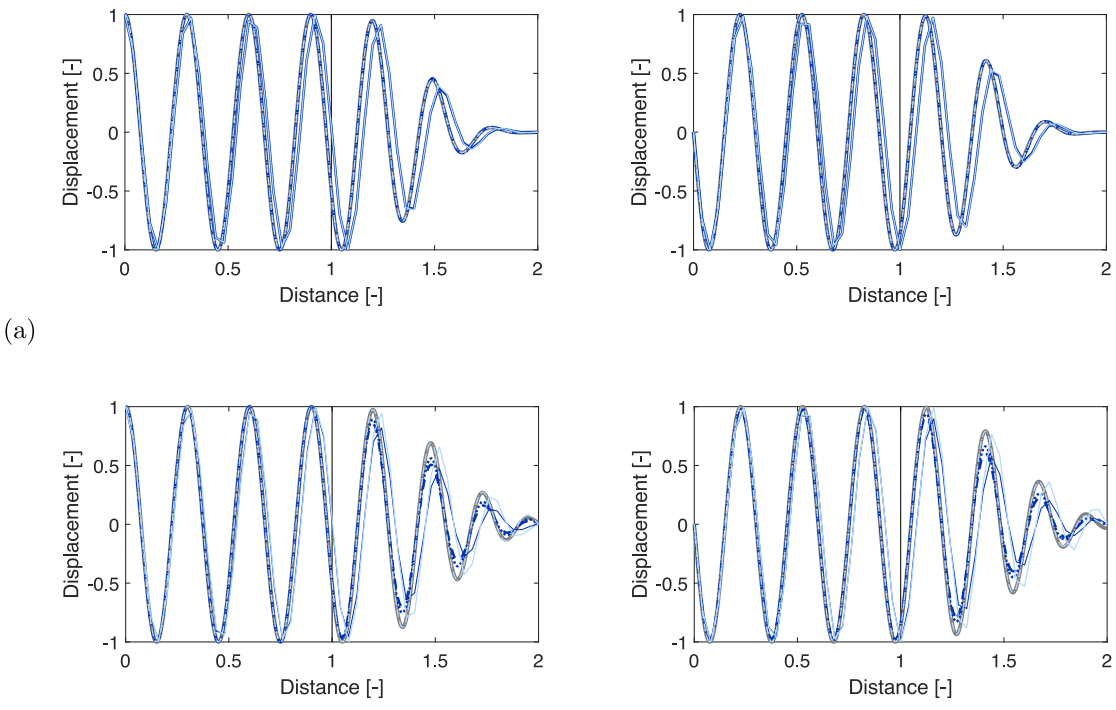

Fig. 7. Real (left) and imaginary (right) part of the normalized displacement in a 1D bar for (a) $f_0 = 0\,\text{Hz}$ and (b) $f_0 = 10\,\text{Hz}$. The reference solution (thick gray line) is compared with the numerical solution, as obtained with Q41 (solid dark blue), Q44 (solid light blue), Q81 (dashed dark blue), Q88 (dashed light blue), T61 (dotted dark blue), and T66 (dotted light blue) elements.

4.2. 2D wave propagation in a homogeneous halfspace

Next, the response of a homogeneous halfspace under 2D plane strain conditions is computed by means of the 2.5D CFS-PML formulation and compared with the reference solution as computed with the direct stiffness method [54]. The halfspace is characterized by a shear wave velocity $C_\text{s} = 150\,\text{m/s}$, a compressional wave velocity $C_\text{p} = 300\,\text{m/s}$, and a density $\rho = 1800\,\text{kg/m}^3$. A damping ratio $D_\text{s} = D_\text{p} = 0.02$ is assumed, where a hysteretic damping model is adopted by introducing complex-valued stiffness moduli, resulting in frequency-independent attenuation. The hysteretic damping model is employed in both the physical domain and the PML buffer. The forced vibration response of the halfspace is considered, resulting from a unit harmonic vertical load at its surface, as shown in Fig. 8a.

The halfspace problem is modeled by means of the 2.5D CFS-PML by considering a strip of elements in the (x, z)-plane, as depicted in Fig. 8b. The domain is subdivided into a regular elastic domain (of length L_1) on top of a CFS-PML (of length L_PML), so that $L = L_1 + L_\text{PML}$. Only displacement degrees of freedom in the y-direction and z-direction are retained. At the base, clamped boundary conditions are applied.

In a first case (case A), the regular elastic domain is omitted ($L_1 = 0$), so that $L = L_\text{PML} = 5\,\text{m}$. In a second case (case B), both the elastic layer and the CFS-PML have a size $L_1 = L_\text{PML} = 2.5$ m, corresponding to the same total domain size $L = 5\,\text{m}$. Both a standard PML and a CFS-PML parameterization, with $\alpha_0 = 0$ and a variable β_0 and ω_0 are considered. The strip is modeled using 10 Q81 elements.

Fig. 9 presents the reference solutions for the vertical velocity $v_z(x, k_y, z = 0, \omega)$ in the frequency–wavenumber domain at the surface of a homogeneous halfspace and an elastic layer of height $L = 5\,\text{m}$ clamped at its base. These solutions are computed using the direct stiffness method [54] and serve as reference cases for the subsequent analysis of the performance of the CFS-PML. The halfspace response represents the target behavior that the (CFS-)PML is designed to reproduce, while the elastic layer corresponds to the limiting case of a (CFS-)PML without attenuation, i.e. $\beta_0 \to 0$. We note that a broad wavenumber range is considered to maintain consistency with the figures presented later.

The response of the halfspace (Fig. 9a) is dominated by a Rayleigh wave, characterized by a peak at the Rayleigh wavenumber $\bar{k}_\text{R} = 1.047$, independent of the frequency. In contrast, the elastic layer exhibits a distinct cut-on frequency $f_1 = C_\text{s}/(4L) = 7.5\,\text{Hz}$, i.e. the frequency at which the layer height $L = 5\,\text{m}$ equals one-quarter of the shear wavelength, $\lambda_\text{s} = C_\text{s}/f = 20\,\text{m}$, below which no wave propagation occurs. It should be noted, however, that the resulting fundamental dispersion curve is less excited by the vertical line load under consideration. Additional dispersion branches appear at odd multiples of this fundamental frequency (i.e., at 15 Hz, 22.5 Hz, etc.) and asymptotically approach the Rayleigh wavenumber at high frequency.

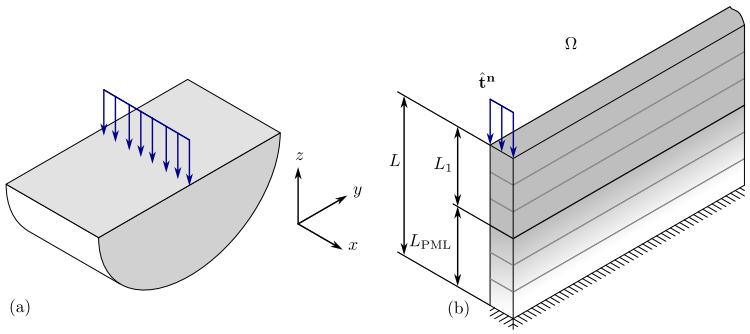

Fig. 8. (a) Forced vibration problem in a halfspace and (b) corresponding 2.5D model.

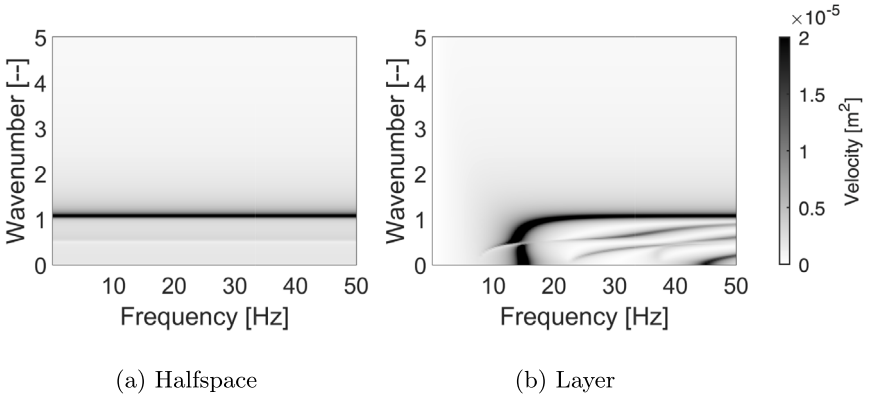

Fig. 9. Reference solution: Modulus of the vertical velocity at the surface of (a) a homogeneous halfspace and (b) a layer with a thickness $L_{\mathrm{PML}} = 5$ m due to unit vertical harmonic loading in the wavenumber-frequency domain, as computed with the direct stiffness method [54].

Fig. 10 shows the response at the top of the layer for case A and the standard PML stretch function, for $\alpha_0 = 0$ and an increasing attenuation parameter β_0. If no attenuation is present (Fig. 10a, $\beta_0 = 0$), the response corresponds to an elastic layer clamped at its base. As the parameter β_0 increases, the response of the PML at higher frequencies corresponds to the homogeneous halfspace, as intended. At lower frequencies, the PML solution diverges significantly from the elastic halfspace solution and is increasingly affected by non-physical artifacts at large wavenumbers. This occurs below 15 Hz, i.e. the second cut-on frequency of the elastic layer, where more spurious modes occur for an increasing value of the parameter β_0.

Introducing a frequency shift in the CFS-PML effectively mitigates the deviations exhibited by the standard PML at low frequencies. Fig. 11 illustrates the surface response for case A for the CFS-PML for $\beta_0 = 20C_s/L_{\mathrm{PML}}$ and increasing values of the frequency-shift parameter ω_0. When a moderate frequency shift of 5 Hz is applied, the spurious reflections that dominate the standard PML at low frequencies are sufficiently attenuated, while the response above approximately 5 Hz still closely follows that of the elastic halfspace. Increasing the frequency shift beyond this point, however, adversely affects the attenuation characteristics of the PML. Large values of ω_0 lead to excessive damping within the medium-frequency range, causing the PML to deviate from the desired halfspace behavior and reducing its effectiveness. Based on these observations, a practical guideline is to select the frequency shift at roughly two-thirds of the cut-on frequency of the corresponding elastic layer, ensuring a balanced compromise between low-frequency stability and accurate wave absorption at higher frequencies.

For case B, i.e. with the domain split into an elastic layer of thickness $L_1 = 2.5$ m on top of a (CFS-)PML layer of the same thickness $L_{\mathrm{PML}} = 2.5$ m, Figs. 12 and 13 present the corresponding surface response for, respectively, an increasing attenuation parameter β_0 (standard PML, $\omega_0 = 0$) and an increasing frequency shift ω_0 (CFS-PML, $\beta_0 = 20\,C_s/L_{\mathrm{PML}}$).

The cut-on frequency of the layered configuration coincides with that of Fig. 9b, which reproduces the response of a 5 m-thick clamped elastic layer: since this cut-on frequency depends only on the total clamped depth $L = L_1 + L_{\mathrm{PML}} = 5$ m, it is unaffected by the change in PML placement. More generally, this cut-on frequency is a property of the clamped system as a whole, i.e. of the total depth L over which the model is clamped, rather than of the PML formulation or its parameters. It can therefore only be shifted to a lower value by considering a deeper domain or by introducing a real coordinate stretch ($\alpha_0 > 0$), both of which increase the number of elements, and hence degrees of freedom, required in the computation.

For the standard PML, comparing Fig. 12 with Fig. 10 depicts similar behavior, where spurious low-frequency artifacts are more apparent as β_0 increases. Since β_0 is defined through Eq. (85) as $a\,C_s/L_{\mathrm{PML}}$, halving L_{PML} at fixed a leaves the depth-integrated

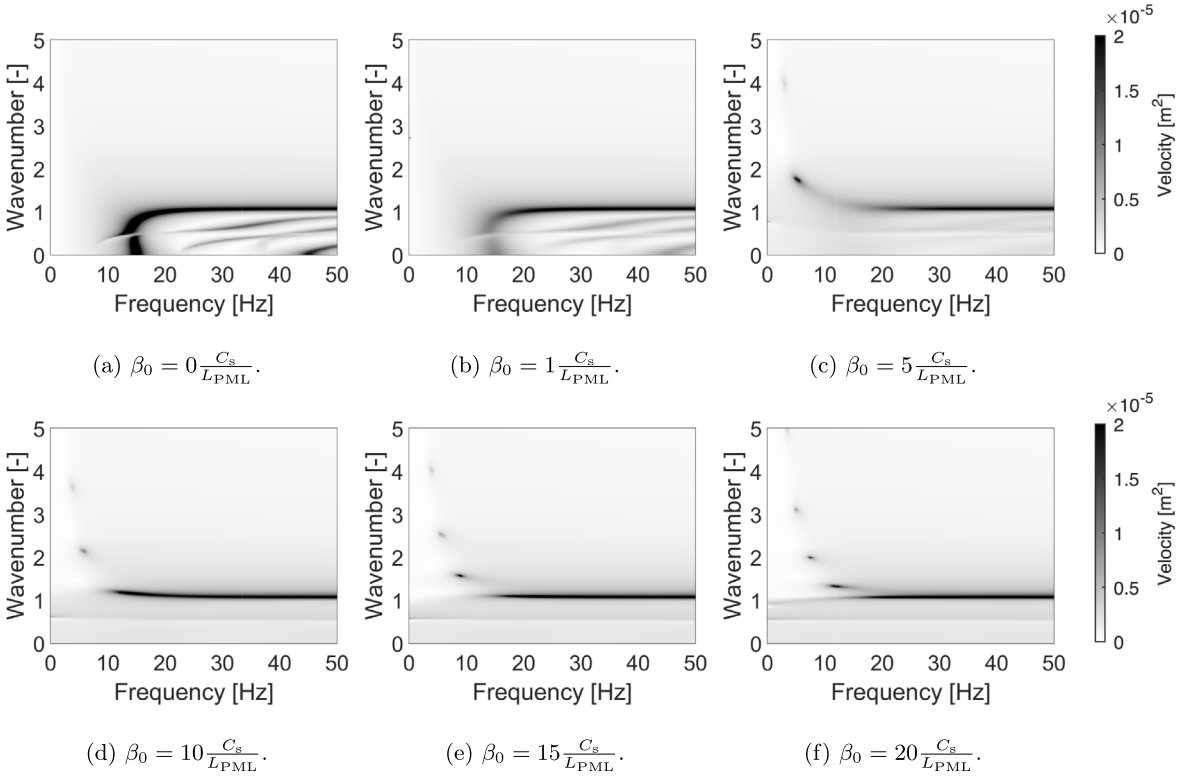

(a) $\beta_0 = 0\frac{C_s}{L_{PML}}$. (b) $\beta_0 = 1\frac{C_s}{L_{PML}}$. (c) $\beta_0 = 5\frac{C_s}{L_{PML}}$.

(d) $\beta_0 = 10\frac{C_s}{L_{PML}}$. (e) $\beta_0 = 15\frac{C_s}{L_{PML}}$. (f) $\beta_0 = 20\frac{C_s}{L_{PML}}$.

Fig. 10. Modulus of the vertical velocity in case A for the standard PML due to unit vertical harmonic loading for an increasing value of the parameter β_0.

attenuation $\int_0^{L_{PML}} \beta_s \, ds = a C_s$ unchanged, so the two configurations apply a comparable overall attenuation. At $\beta_0 = 20 C_s/L_{PML}$, however, the layered configuration exhibits fewer distinct spurious peaks than the original PML strip spanning the full 5 m, and at a different point in the (f, k_y) domain. This indicates that the discrepancies stem from the reduced extent of the PML and its interaction with the wave reflected at the clamped base.

For the CFS-PML, Fig. 13 confirms that introducing a frequency shift is equally effective at mitigating these low-frequency artifacts. A moderate shift of $\omega_0 = 2\pi \times 5$ Hz again suppresses the spurious reflections while preserving accurate wave absorption above approximately 5 Hz, consistent with the conclusions drawn from Fig. 11.

4.3. 3D wave propagation in a shallow domain

The two-dimensional examples of Section 4.2 already probe the full range of propagating and evanescent longitudinal wavenumbers, including near-grazing incidence (i.e. the response at large longitudinal wavenumbers), but restrict the CFS-PML stretching to the vertical z direction only. The performance of the (CFS-)PML under near-grazing incidence is further demonstrated for a shallow, laterally-truncated 3D domain, as depicted in Fig. 14. The domain has the same total depth $L_1 + L_{PML} = 5$ m and the same partition of an elastic layer with a thickness $L_1 = 2.5$ m and a (CFS-)PML with a thickness $L_{PML} = 2.5$ m as previously examined in the 2D layered configuration (case B) of Section 4.2 (Figs. 12 and 13), and the same soil properties and corresponding cut-on frequencies. The domain is truncated laterally at $x = 100$ m by a PML of the same thickness $L_{PML} = 2.5$ m. A unit vertical harmonic point load is applied at the free surface at the symmetry axis $x = y = 0$, and the domain is discretized with elements with a size of 0.5 m. The frequency–wavenumber response is computed on a grid combining 500 wavenumbers linearly spaced over $\bar{k}_y = k_y C_s/\omega \in [0, 5]$, with 10 wavenumbers logarithmically spaced over $\bar{k}_y \in [5, 10^3]$ to represent the strongly evanescent near-field content at large wavenumber. The spatial response is obtained through an inverse wavenumber transform evaluated at receivers $y = 1, \ldots, 100$ m. The response is computed for a standard PML ($\beta_0 = 20 C_s/L_{PML}$, $\omega_0 = 0$) and a CFS-PML with the same attenuation parameter and a frequency shift $\omega_0 = 2\pi \times 5$ Hz, at four excitation frequencies (2, 5, 10 and 20 Hz), and compared to the reference solution of the true, unbounded homogeneous halfspace, computed with the direct stiffness method [54].

Fig. 15 compares the modulus of the vertical surface velocity obtained with the standard PML and the CFS-PML to the reference halfspace solution. At 2 Hz, below f_1, the standard PML response is dominated by the same low-frequency spurious artifacts identified for the PML in Section 4.2. At 5 Hz, the standard PML response remains dominated by these spurious artifacts, whereas the

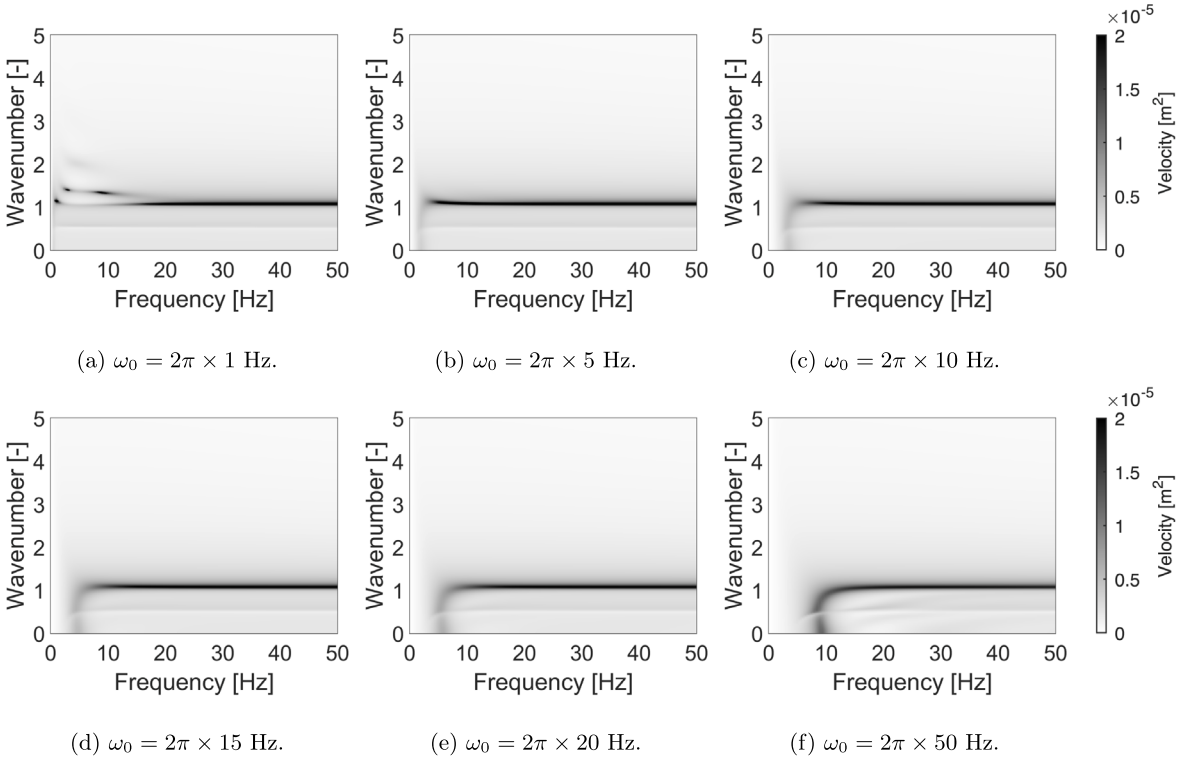

(a) $\omega_0 = 2\pi \times 1$ Hz. (b) $\omega_0 = 2\pi \times 5$ Hz. (c) $\omega_0 = 2\pi \times 10$ Hz.

(d) $\omega_0 = 2\pi \times 15$ Hz. (e) $\omega_0 = 2\pi \times 20$ Hz. (f) $\omega_0 = 2\pi \times 50$ Hz.

Fig. 11. Modulus of the vertical velocity in case A for the CFS-PML due to unit vertical harmonic loading for an increasing value of the frequency shift ω_0.

CFS-PML already agrees well with the reference wavefield. At 2 Hz, by contrast, the CFS-PML response is somewhat overdamped, with a stronger spatial decay than in the reference solution, as a direct consequence of exciting the CFS-PML below its shift frequency.

At 10 Hz, the CFS-PML continues to match the reference solution. The standard PML, however, still exhibits pronounced non-physical interference: a persistent, high-amplitude oblique fringe pattern that does not decay with distance from the source, characteristic of spurious reflections from the lateral and corner PML regions rather than of true wave attenuation. This confirms that, in this laterally truncated, near-grazing-incidence configuration, the standard PML's low-frequency deficiency persists up to the second cut-on frequency, consistent with the conclusions from Section 4.2. Only at 20 Hz do both PML and CFS-PML formulations converge to the reference wavefield, consistent with the earlier observation that spurious PML modes are confined to the low-frequency range dominated by evanescent and near-grazing wave content. These observations are consistent with the two-dimensional layered results of Figs. 12 and 13.

4.4. Wave propagation along a cut-and-cover tunnel

In a fourth numerical example, the dynamic soil–structure interaction problem of a tunnel embedded in a semi-infinite soil medium is investigated. The tunnel consists of a reinforced concrete rectangular cross-section with outer dimensions of 16 m × 8 m and a uniform wall thickness of 1 m, as illustrated in Fig. 16. The tunnel is assumed to be constructed using a cut-and-cover technique in a sloped trench. After installation of the tunnel structure, the trench is backfilled, resulting in a soil cover above and around the tunnel. The vertical soil cover above the tunnel amounts to 2 m. The material properties for the soil, the backfill and the concrete are summarized in Table 1.

In order to model wave radiation into the far field, the computational domain is truncated using PMLs at the lateral and bottom boundaries, while a free surface is retained at the ground level. A vertical harmonic point load P is applied centrally at the tunnel invert.

The cross-section is discretized using quadratic six-node triangular elements with a target element size of 1 m, as illustrated in Fig. 17. This discretization results in a two-dimensional mesh comprising 6778 nodes and 3284 elements. Boundary conditions are imposed by fully constraining all displacements along the left, right, and bottom edges of the domain. The total number of degrees of freedom, considering this mesh, for the classical PML and the CFS-PML amount 19671 and 33975 respectively, corresponding to a 72.7% relative increase for the CFS-PML formulation.

The response of the tunnel–soil system due to the vertical harmonic load at the tunnel invert is evaluated in the frequency range from 1 to 50 Hz using a frequency increment of 0.5 Hz. The dimensionless wavenumber $\bar{k}_y$ is uniformly sampled between $\bar{k}_y = 0$

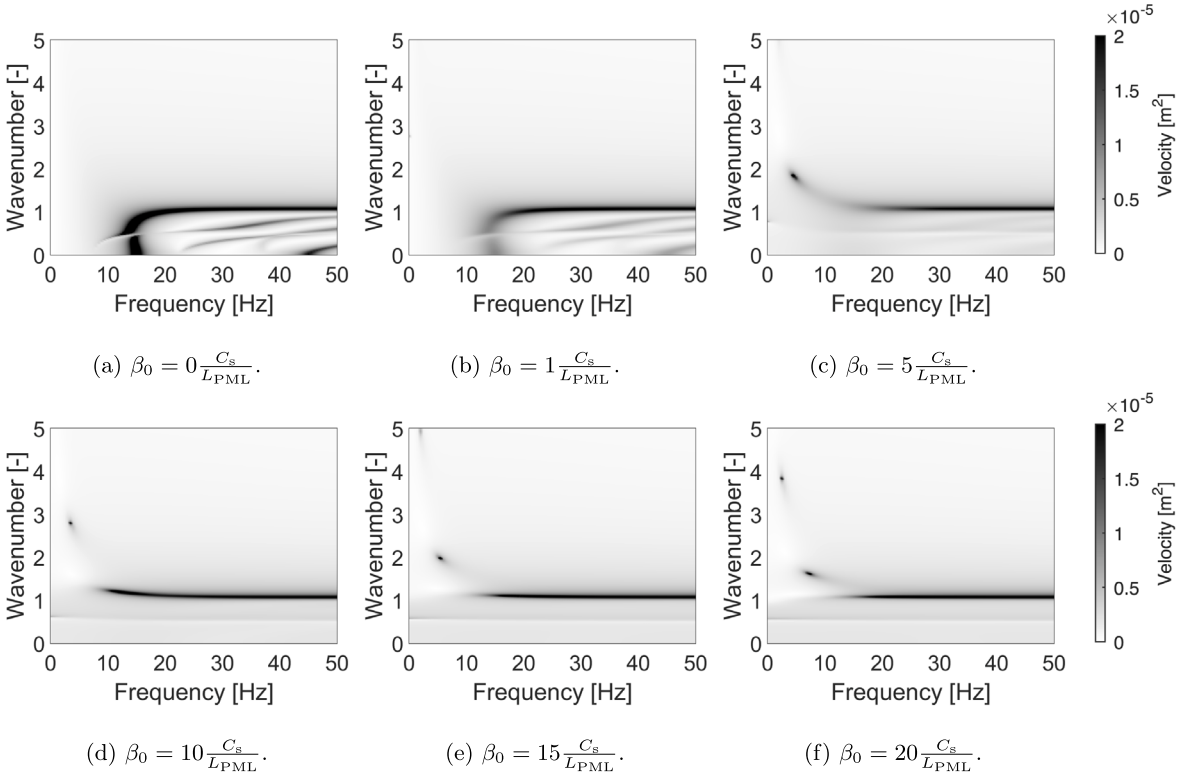

(a) $\beta_0 = 0\frac{C_s}{L_{PML}}$. (b) $\beta_0 = 1\frac{C_s}{L_{PML}}$. (c) $\beta_0 = 5\frac{C_s}{L_{PML}}$.

(d) $\beta_0 = 10\frac{C_s}{L_{PML}}$. (e) $\beta_0 = 15\frac{C_s}{L_{PML}}$. (f) $\beta_0 = 20\frac{C_s}{L_{PML}}$.

Fig. 12. Modulus of the vertical velocity at the surface of an elastic layer ($L_1 = 2.5\,\text{m}$) on a standard PML ($L_{PML} = 2.5\,\text{m}$) due to unit vertical harmonic loading for an increasing value of the parameter β_0.

Table 1
Material properties for the cut-and-cover tunnel problem.

Material	C_s [m/s]	C_p [m/s]	ρ [kg/m^3]	D_s [-]	D_p [-]
Soil	150	300	1800	0.02	0.02
Backfill	100	200	1800	0.02	0.02
Concrete	2236	3652	2500	0.02	0.02

and $\bar{k}_y = 1$ using 200 sampling points. Fig. 18 shows the resulting frequency–wavenumber content of the vertical displacement at receiver points A and B.

To aid the interpretation of these diagrams, two reference dispersion curves associated with bending-wave propagation are included. The first represents the free bending wave of the tunnel, considering a rigid cross-section. In this idealization, the tunnel is modeled as an Euler–Bernoulli beam with cross-sectional area A and second moment of area I, where the corresponding bending-wave dispersion relation is given as

$$k_{b,tunnel} = \left(\frac{\rho A}{EI}\right)^{1/4} \omega^{1/2}. \tag{91}$$

A second reference curve is obtained by considering bending-wave propagation in an equivalent plate of thickness $h = 1$ m, corresponding to the tunnel wall thickness. The plate bending stiffness is given by

$$D = \frac{Eh^3}{12\left(1-\nu^2\right)}, \tag{92}$$

and the associated bending-wave dispersion relation is

$$k_{b,plate} = \left(\frac{\rho h}{D}\right)^{1/4} \omega^{1/2}. \tag{93}$$

These two reference curves highlight the characteristic dispersion behavior of global bending of the tunnel cross-section and local bending of the tunnel wall.

As shown in Fig. 18, the frequency–wavenumber spectra at receivers A and B are dominated by a dispersive wave propagation associated with local plate-type bending of the tunnel invert. At low frequencies, the response is evanescent, where the global

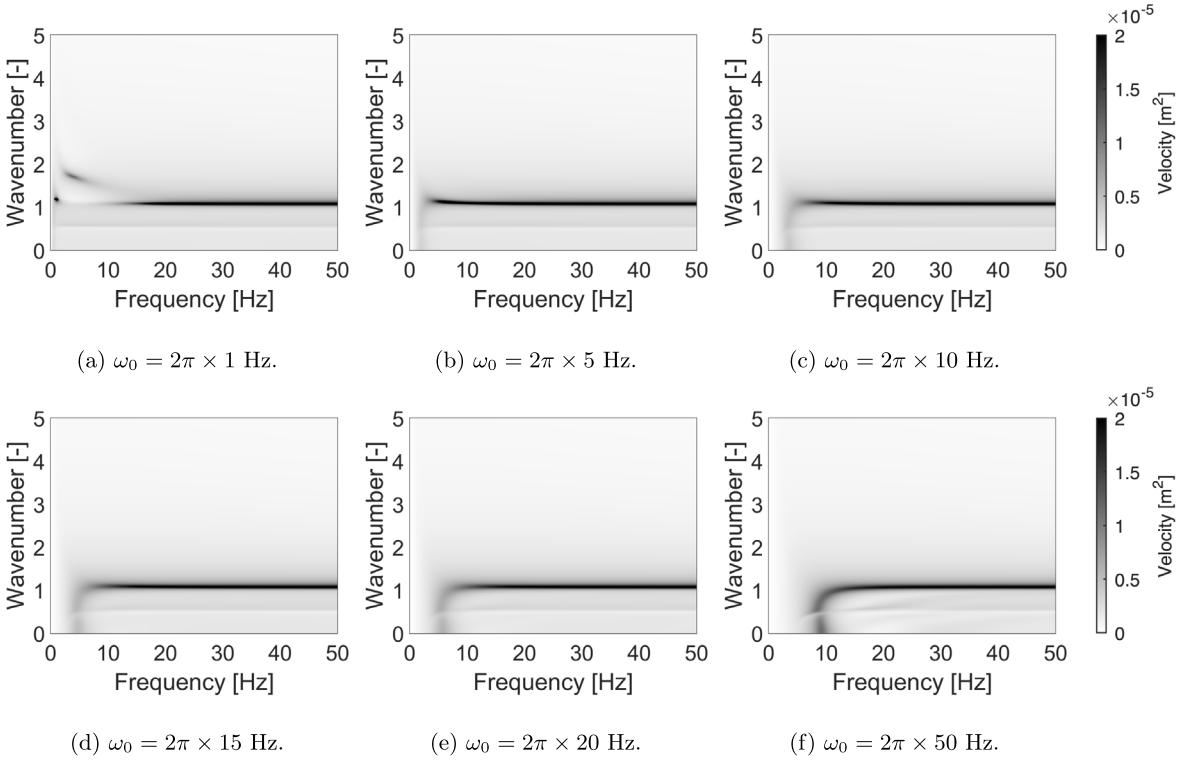

Fig. 13. Modulus of the vertical velocity at the surface of an elastic layer ($L_1 = 2.5\,\mathrm{m}$) on a CFS-PML ($L_{\mathrm{PML}} = 2.5\,\mathrm{m}$, $\beta_0 = 20\,C_s/L_{\mathrm{PML}}$) due to unit vertical harmonic loading for an increasing value of the frequency shift ω_0.

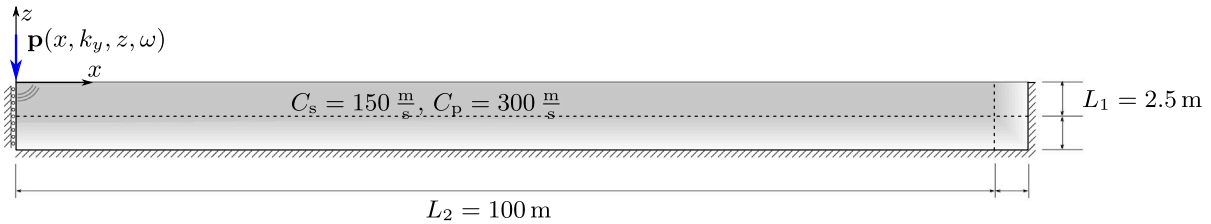

Fig. 14. Shallow domain geometry: an elastic layer of thickness $L_1 = 2.5\,\mathrm{m}$ overlying a PML of thickness $L_{\mathrm{PML}} = 2.5\,\mathrm{m}$, truncated laterally at $x = 100\,\mathrm{m}$ by a second PML of the same thickness. A unit vertical harmonic point load is applied at the origin $x = y = z = 0$ of the coordinate system.

bending of the tunnel cross-section is not excited. A distinct cut-on frequency appears at approximately 7.5 Hz, corresponding to the onset of a guided plate-bending mode at the tunnel invert. Above this threshold, a clearly identifiable wave dispersion progressively approaches the analytical reference curve for a free bending wave at the invert.

The spatial response is subsequently obtained through inverse wavenumber transform from the wavenumber k_y to the spatial coordinate y, resulting in the wave fields as shown in Fig. 19.

An overview of the computational cost associated with both the displacement-based formulation and the CFS-PML model is presented in Table 2.[1] Global assembly time denotes the computational effort required to construct the frequency- and wavenumber-independent system matrices. For the CFS-PML, the entire system can be assembled upfront, whereas for the classical PML only the matrices associated with the interior domain are frequency–wavenumber independent and can therefore be preassembled. Dynamic assembly time represents the additional computational effort needed to reconstruct the frequency–wavenumber dependent components of the system matrices. This reassembly step is required in the displacement-based PML formulation, where the stretch

[1] Computations were carried out on an HP Dragonfly laptop equipped with a 13th-generation Intel Core i7-1355U processor, operating at a base frequency of 1.70 GHz. All results reported in this work were obtained using a single computational thread, ensuring that the observed timings reflect the algorithmic performance of the FE formulation.

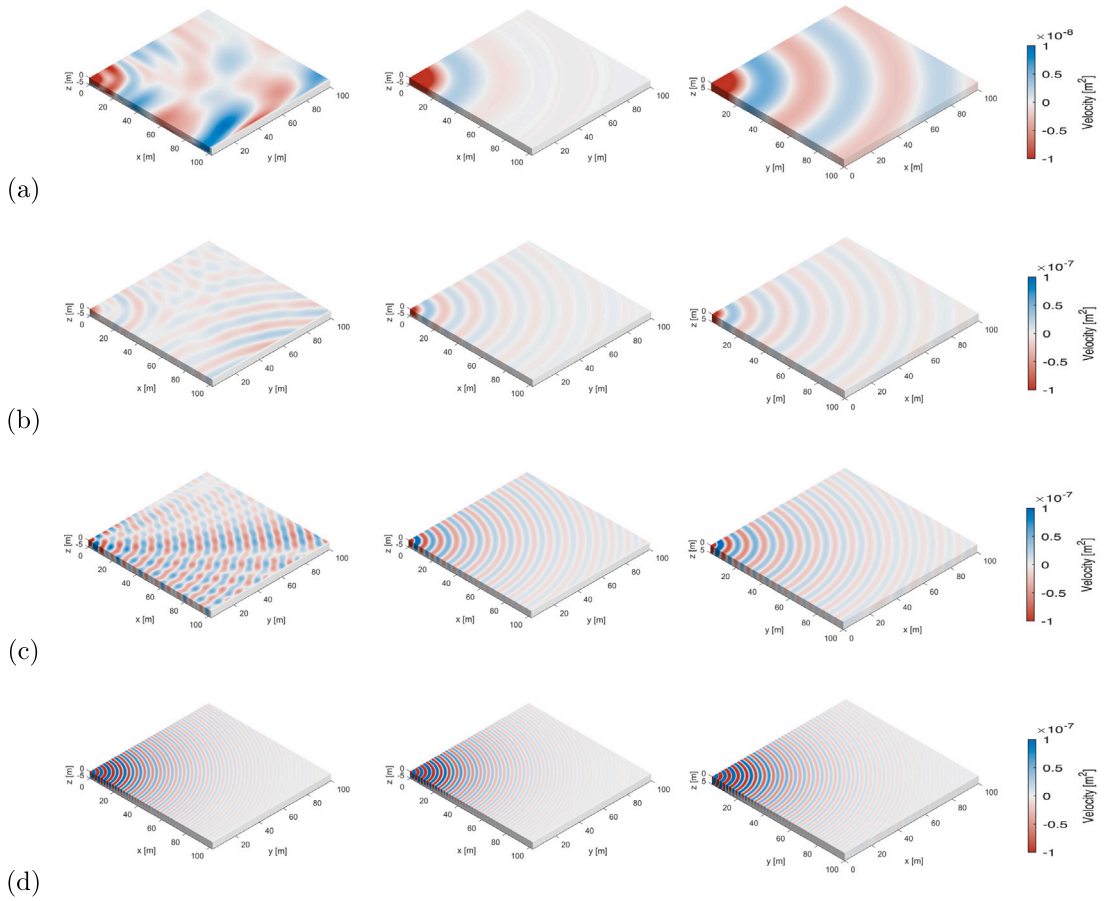

Fig. 15. Real part of the vertical velocity at the surface of the standard PML (left) and the CFS-PML (center) due to unit vertical harmonic loading at (a) 2 Hz, (b) 5 Hz, (c) 10 Hz, and (d) 20 Hz. The reference halfspace solution is also plotted (right).

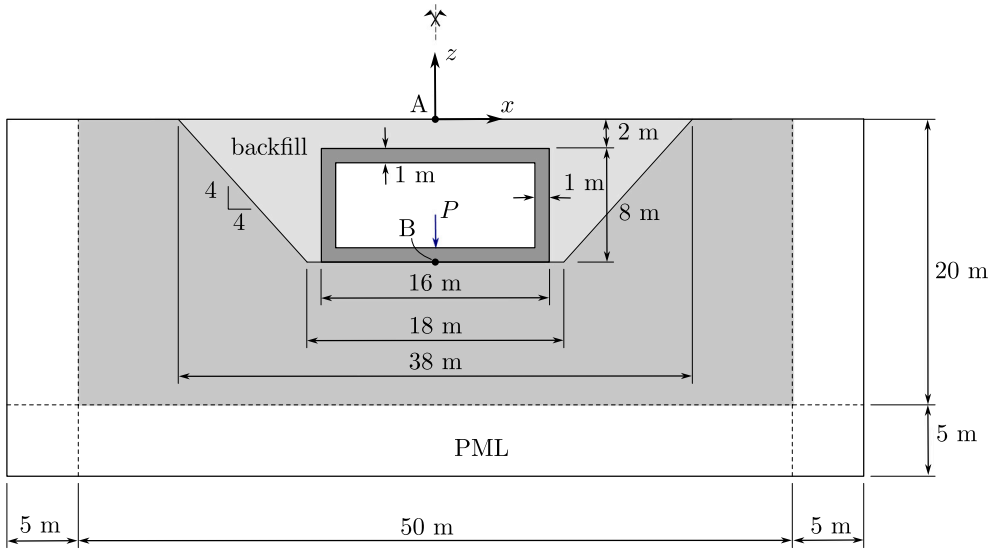

Fig. 16. Geometry of the cut-and-cover tunnel problem.

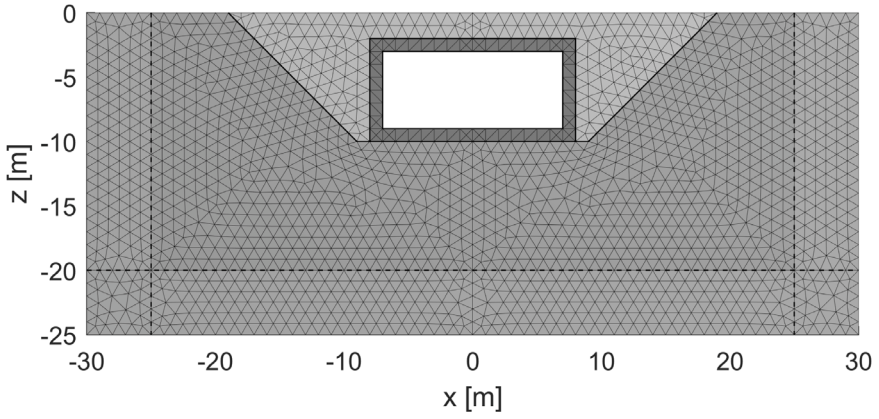

Fig. 17. FE mesh for the cut-and-cover tunnel problem.

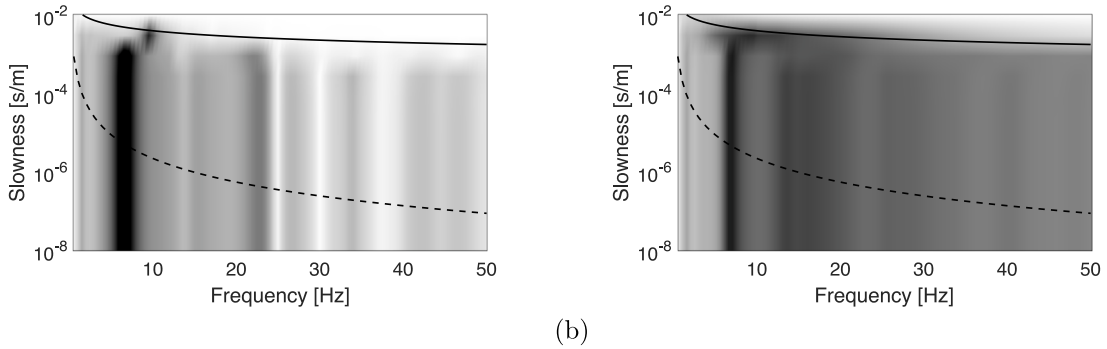

Fig. 18. Vertical displacement in the frequency–wavenumber domain at points (a) A and (b) B for a vertical load applied at the tunnel invert. The dispersion curves corresponding to the bending wave of the tunnel considered as a rigid cross-section (dashed line) and to a plate bending wave (solid line) are also included.

Table 2
Comparison of wall-clock time between the displacement-based 2.5D PML and the 2.5D CFS-PML.

PML type	Assembly [s]		Solution [s]	Total [s]
	Global	Dynamic		
Displacement-based	1.2	10821.7	3679.2	14 502.1
CFS-PML	6.6	–	5289.0	5295.6

functions depend on frequency and longitudinal wavenumber and enter directly into the element matrices. As a result, the matrices must be integrated and assembled for each frequency–wavenumber pair. In contrast, the computational advantage of the proposed formulation stems from the auxiliary-field reformulation, which yields frequency- and wavenumber-independent matrices that are assembled only once. The solution time corresponds to the accumulated time needed to solve the dynamic system of equations across all frequencies and wavenumbers, and the total computational time is obtained as the sum of the assembly and solution times. Parallelizing the assembly loop across multiple cores is a complementary optimization step that reduces the cost of assembling a given set of matrices, with a speedup bounded by the number of available cores, whereas the auxiliary-field reformulation removes the need to reassemble matrices for each frequency–wavenumber pair altogether. As a result, the computational benefit scales with the size of the frequency–wavenumber sampling. A related observation was made for a constant-matrix, auxiliary-field CFS-PML formulation in the time domain [44], where avoiding repeated per-step evaluations was likewise the primary source of the reported computational savings.

Table 2 shows that the dynamic assembly time required for the classical PML constitutes the major portion of the overall computational cost. Because the frequency- and wavenumber-dependent parts of the system matrices must be reconstructed for every evaluation point, the classical PML experiences a significant overhead that scales directly with the number of frequencies and

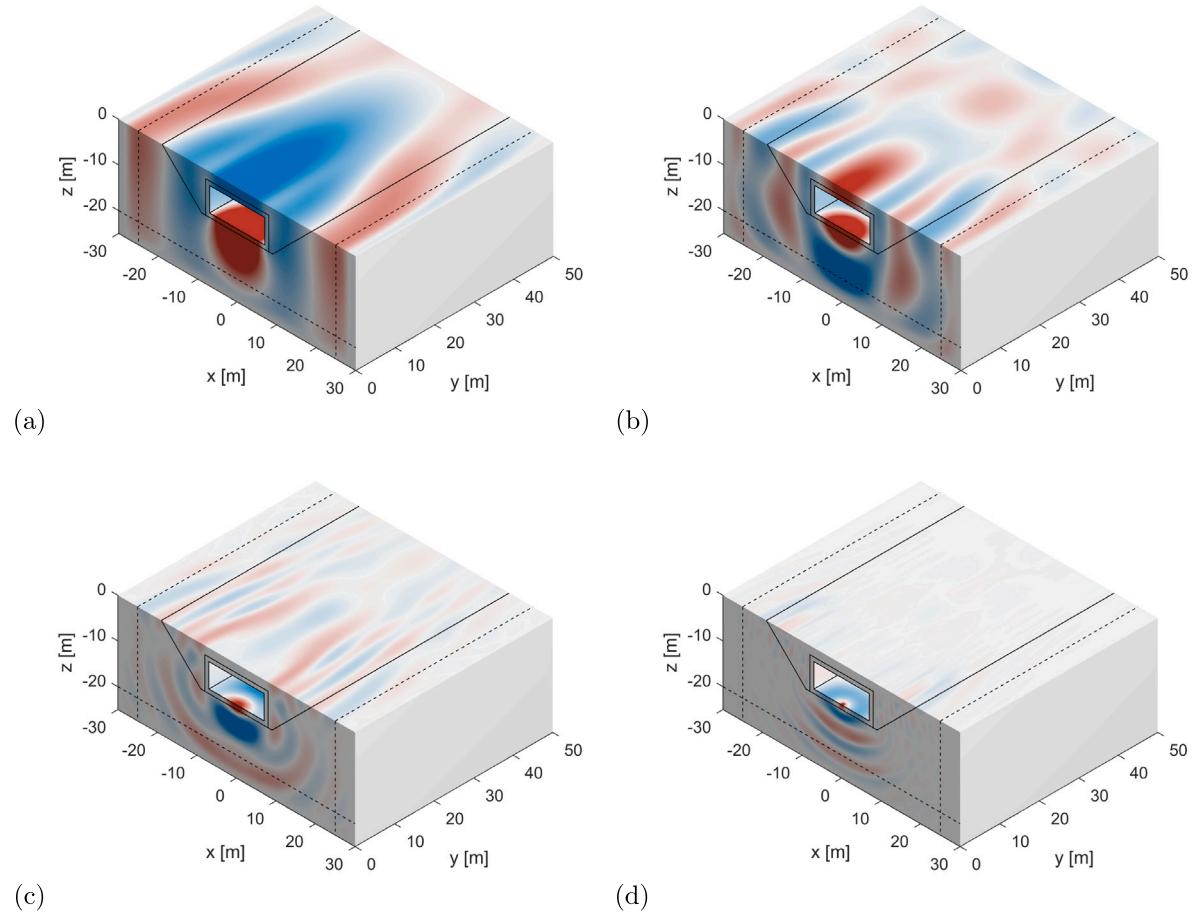

Fig. 19. Real part of the vertical harmonic displacement at a frequency of (a) 5 Hz, (b) 10 Hz, (c) 20 Hz, and (d) 50 Hz.

wavenumbers considered. In contrast, the CFS-PML formulation avoids this repeated assembly altogether, which leads to a markedly reduced computational time. Although the CFS-PML introduces a modest increase in the number of degrees of freedom, this has no noticeable impact on the solution time. The linear systems to be solved remain of comparable size and conditioning, and the absence of dynamic assembly compensates for the slightly larger system. As a result, the CFS-PML achieves a lower total computational time despite the increase in DOF count.

5. Conclusions

In this paper, a 2.5D CFS-PML has been derived in the context of the 2.5D FE technique. By incorporating auxiliary fields, the formulation produces system matrices that are independent of both frequency and longitudinal wavenumber. Consequently, the global matrices need to be assembled only once, and the governing equations reduce to a matrix polynomial in the combined wavenumber–frequency domain. This eliminates the repeated matrix reassembly required in classical 2.5D PML approaches and leads to a substantial gain in computational efficiency.

The complex frequency shift of the CFS-PML enhances the attenuation of low-frequency waves and waves impinging at grazing incidence, mitigating well-known deficiencies of the standard PML. The method preserves the perfect matching property and provides robust absorption performance over a broad range of frequencies. The choice of interpolation for the auxiliary variables offers flexibility: using the same interpolation order as the displacement field improves accuracy, whereas reduced-order interpolations provide a computationally more economical alternative without compromising overall absorption.

The resulting matrix polynomial structure of the 2.5D system of equations enables efficient broadband simulations, dispersion analysis via quadratic eigenvalue problems, and integration with model-order reduction techniques.

CRediT authorship contribution statement

Stijn François: Writing – review & editing, Writing – original draft, Visualization, Validation, Supervision, Software, Resources, Project administration, Methodology, Investigation, Funding acquisition, Formal analysis, Conceptualization. **Amar Pashov:** Writing

– review & editing, Writing – original draft, Visualization, Validation, Software, Investigation, Conceptualization. **Loukas F. Kallivokas:** Writing – review & editing, Methodology, Conceptualization. **Geert Degrande:** Writing – review & editing, Writing – original draft, Supervision, Resources, Project administration, Methodology, Investigation, Funding acquisition, Conceptualization.

Acknowledgments

The results presented in this work were obtained within the project "Model Order Reduction Techniques for the Prediction of Railway-Induced Vibrations in the Built Environment", funded by the Research Council of KU Leuven (Project No. C14/20/073). Additional support was provided by the Research Foundation Flanders (FWO) through doctoral fellowship 1118125N awarded to Amar Pashov and research project G021426N. The authors gratefully acknowledge the financial support of KU Leuven and FWO.

Declaration of competing interest

The authors declare the following financial interests/personal relationships which may be considered as potential competing interests: Amar Pashov reports financial support was provided by Research Foundation Flanders. The other authors declare that they have no known competing financial interests or personal relationships that could have appeared to influence the work reported in this paper.

Appendix. System matrices

In this appendix, expressions for the components of the system matrices in (73) to (77) are given:

$$\mathbf{K}_{0\mathrm{uu}} = \frac{\alpha_z}{\alpha_x}\mathbf{B}_x^{\mathrm{T}}\mathbf{C}\mathbf{B}_x + \frac{\alpha_x}{\alpha_z}\mathbf{B}_z^{\mathrm{T}}\mathbf{C}\mathbf{B}_z + \mathbf{B}_x^{\mathrm{T}}\mathbf{C}\mathbf{B}_z + \mathbf{B}_z^{\mathrm{T}}\mathbf{C}\mathbf{B}_x + \rho a_0\mathbf{N}_{\mathrm{u}}^{\mathrm{T}}\mathbf{N}_{\mathrm{u}} \tag{A.1}$$

$$\mathbf{C}_{0\mathrm{uu}} = \rho a_1\mathbf{N}_{\mathrm{u}}^{\mathrm{T}}\mathbf{N}_{\mathrm{u}} \tag{A.2}$$

$$\mathbf{M}_{0\mathrm{uu}} = \rho a_2\mathbf{N}_{\mathrm{u}}^{\mathrm{T}}\mathbf{N}_{\mathrm{u}} \tag{A.3}$$

$$\mathbf{K}_{0\mathrm{u}\xi} = \mathbf{B}_x^{\mathrm{T}}\mathbf{C}\mathbf{L}_{x0}\mathbf{N}_{\xi} \tag{A.4}$$

$$\mathbf{K}_{0\mathrm{u}\zeta} = \mathbf{B}_z^{\mathrm{T}}\mathbf{C}\mathbf{L}_{z0}\mathbf{N}_{\zeta} \tag{A.5}$$

$$\mathbf{K}_{0\mathrm{u}\upsilon} = \rho a_0\mathbf{N}_{\mathrm{u}}^{\mathrm{T}}\mathbf{N}_{\upsilon} \tag{A.6}$$

$$\mathbf{C}_{0\mathrm{u}\upsilon} = \rho a_1\mathbf{N}_{\mathrm{u}}^{\mathrm{T}}\mathbf{N}_{\upsilon} \tag{A.7}$$

$$\mathbf{M}_{0\mathrm{u}\upsilon} = \rho a_2\mathbf{N}_{\mathrm{u}}^{\mathrm{T}}\mathbf{N}_{\upsilon} \tag{A.8}$$

$$\mathbf{K}_{0\xi\xi} = \gamma_0\mathbf{N}_{\xi}^{\mathrm{T}}\mathbf{N}_{\xi} \tag{A.9}$$

$$\mathbf{C}_{0\xi\xi} = \gamma_1\mathbf{N}_{\xi}^{\mathrm{T}}\mathbf{N}_{\xi} \tag{A.10}$$

$$\mathbf{M}_{0\xi\xi} = \gamma_2\mathbf{N}_{\xi}^{\mathrm{T}}\mathbf{N}_{\xi} \tag{A.11}$$

$$\mathbf{K}_{0\eta\eta} = b_0\mathbf{N}_{\eta}^{\mathrm{T}}\mathbf{N}_{\eta} \tag{A.12}$$

$$\mathbf{C}_{0\eta\eta} = b_1\mathbf{N}_{\eta}^{\mathrm{T}}\mathbf{N}_{\eta} \tag{A.13}$$

$$\mathbf{M}_{0\eta\eta} = b_2\mathbf{N}_{\eta}^{\mathrm{T}}\mathbf{N}_{\eta} \tag{A.14}$$

$$\mathbf{K}_{0\zeta\zeta} = \delta_0\mathbf{N}_{\zeta}^{\mathrm{T}}\mathbf{N}_{\zeta} \tag{A.15}$$

$$\mathbf{C}_{0\zeta\zeta} = \delta_1\mathbf{N}_{\zeta}^{\mathrm{T}}\mathbf{N}_{\zeta} \tag{A.16}$$

$$\mathbf{M}_{0\zeta\zeta} = \delta_2\mathbf{N}_{\zeta}^{\mathrm{T}}\mathbf{N}_{\zeta} \tag{A.17}$$

$$\mathbf{K}_{0\psi\psi} = d_0\mathbf{N}_{\psi}^{\mathrm{T}}\mathbf{N}_{\psi} \tag{A.18}$$

$$\mathbf{C}_{0\psi\psi} = d_1\mathbf{N}_{\psi}^{\mathrm{T}}\mathbf{N}_{\psi} \tag{A.19}$$

$$\mathbf{K}_{0\chi\chi} = c_0\mathbf{N}_{\chi}^{\mathrm{T}}\mathbf{N}_{\chi} \tag{A.20}$$

$$\mathbf{C}_{0\chi\chi} = c_1\mathbf{N}_{\chi}^{\mathrm{T}}\mathbf{N}_{\chi} \tag{A.21}$$

$$\mathbf{K}_{0\upsilon\upsilon} = b_0\mathbf{N}_{\upsilon}^{\mathrm{T}}\mathbf{N}_{\upsilon} \tag{A.22}$$

$$\mathbf{C}_{0\upsilon\upsilon} = b_1\mathbf{N}_{\upsilon}^{\mathrm{T}}\mathbf{N}_{\upsilon} \tag{A.23}$$

$$\mathbf{M}_{0\upsilon\upsilon} = b_2\mathbf{N}_{\upsilon}^{\mathrm{T}}\mathbf{N}_{\upsilon} \tag{A.24}$$

$$\mathbf{K}_{0\xi\mathrm{u}} = \left(\delta_0 - \frac{\alpha_z}{\alpha_x}\gamma_0\right)\mathbf{N}_{\xi}^{\mathrm{T}}\mathbf{L}_{x0}^{\mathrm{T}}\mathbf{B}_x \tag{A.25}$$

$$\mathbf{C}_{0\xi\mathrm{u}} = \left(\delta_1 - \frac{\alpha_z}{\alpha_x}\gamma_1\right)\mathbf{N}_{\xi}^{\mathrm{T}}\mathbf{L}_{x0}^{\mathrm{T}}\mathbf{B}_x \tag{A.26}$$

$$\mathbf{M}_{0\xi u} = \left(\delta_2 - \frac{\alpha_z}{\alpha_x}\gamma_2\right)\mathbf{N}_\xi^{\mathrm{T}}\mathbf{L}_{x0}^{\mathrm{T}}\mathbf{B}_x \tag{A.27}$$

$$\mathbf{K}_{0\eta u} = \left(a_0 - \alpha_x\alpha_z b_0\right)\mathbf{N}_\eta^{\mathrm{T}}\mathbf{N}_u \tag{A.28}$$

$$\mathbf{C}_{0\eta u} = \left(a_1 - \alpha_x\alpha_z b_1\right)\mathbf{N}_\eta^{\mathrm{T}}\mathbf{N}_u \tag{A.29}$$

$$\mathbf{M}_{0\eta u} = \left(a_2 - \alpha_x\alpha_z b_2\right)\mathbf{N}_\eta^{\mathrm{T}}\mathbf{N}_u \tag{A.30}$$

$$\mathbf{K}_{0\zeta u} = \left(\gamma_0 - \frac{\alpha_x}{\alpha_z}\delta_0\right)\mathbf{N}_\zeta^{\mathrm{T}}\mathbf{L}_{z0}^{\mathrm{T}}\mathbf{B}_z \tag{A.31}$$

$$\mathbf{C}_{0\zeta u} = \left(\gamma_1 - \frac{\alpha_x}{\alpha_z}\delta_1\right)\mathbf{N}_\zeta^{\mathrm{T}}\mathbf{L}_{z0}^{\mathrm{T}}\mathbf{B}_z \tag{A.32}$$

$$\mathbf{M}_{0\zeta u} = \left(\gamma_2 - \frac{\alpha_x}{\alpha_z}\delta_2\right)\mathbf{N}_\zeta^{\mathrm{T}}\mathbf{L}_{z0}^{\mathrm{T}}\mathbf{B}_z \tag{A.33}$$

$$\mathbf{K}_{0\psi u} = \beta_z\mathbf{N}_\psi^{\mathrm{T}}\mathbf{N}_u \tag{A.34}$$

$$\mathbf{K}_{0\chi u} = \beta_x\mathbf{N}_\chi^{\mathrm{T}}\mathbf{N}_u \tag{A.35}$$

$$\mathbf{K}_{0uu} = (0 - b_0)\mathbf{N}_u^{\mathrm{T}}\mathbf{N}_u \tag{A.36}$$

$$\mathbf{C}_{0uu} = (0 - b_1)\mathbf{N}_u^{\mathrm{T}}\mathbf{N}_u \tag{A.37}$$

$$\mathbf{M}_{0uu} = (1 - b_2)\mathbf{N}_u^{\mathrm{T}}\mathbf{N}_u \tag{A.38}$$

$$\mathbf{K}_{1uu} = \alpha_z\mathbf{B}_x^{\mathrm{T}}\mathbf{C}\mathbf{L}_{y0}\mathbf{N}_u - \alpha_z(\mathbf{L}_{y0}\mathbf{N}_u)^{\mathrm{T}}\mathbf{C}\mathbf{B}_x + \alpha_x\mathbf{B}_z^{\mathrm{T}}\mathbf{C}\mathbf{L}_{y0}\mathbf{N}_u - \alpha_x(\mathbf{L}_{y0}\mathbf{N}_u)^{\mathrm{T}}\mathbf{C}\mathbf{B}_z \tag{A.39}$$

$$\mathbf{K}_{1u\psi} = \mathbf{B}_x^{\mathrm{T}}\mathbf{C}\mathbf{L}_{y0}\mathbf{N}_\psi - (\mathbf{L}_{y0}\mathbf{N}_u)^{\mathrm{T}}\mathbf{C}\mathbf{L}_x\mathbf{N}_\psi \tag{A.40}$$

$$\mathbf{K}_{1u\chi} = \mathbf{B}_z^{\mathrm{T}}\mathbf{C}\mathbf{L}_{y0}\mathbf{N}_\chi - (\mathbf{L}_{y0}\mathbf{N}_u)^{\mathrm{T}}\mathbf{C}\mathbf{L}_z\mathbf{N}_\chi \tag{A.41}$$

$$\mathbf{K}_{2uu} = \alpha_x\alpha_z(\mathbf{L}_{y0}\mathbf{N}_u)^{\mathrm{T}}\mathbf{C}\mathbf{L}_{y0}\mathbf{N}_u \tag{A.42}$$

$$\mathbf{K}_{2u\eta} = (\mathbf{L}_{y0}\mathbf{N}_u)^{\mathrm{T}}\mathbf{C}\mathbf{L}_{y0}\mathbf{N}_\eta \tag{A.43}$$

Data availability

Data will be made available on request.

References

[1] R. Hwang, J. Lysmer, Response of buried structures to traveling waves, J. Geotech. Geoenvironmental Eng. Proc. ASCE 107 (GT2) (1981) 183–200.
[2] Y. Yang, H. Hung, A 2.5D finite-infinite element approach for modelling visco-elastic bodies subjected to moving loads, Internat. J. Numer. Methods Engrg. 51 (2001) 1317–1336.
[3] L. Karl, T. Fechner, M. Schevenels, S. François, G. Degrande, Geotechnical characterization of a river dyke by surface waves, Near Surf. Geophys. 9 (6) (2011) 515–527.
[4] E. Kausel, J.M. de Oliveira Barbosa, Analysis of embankment underlain by elastic half-space: 2.5D model with paralongitudinal approximations to the half-space, Soil Dyn. Earthq. Eng. 155 (2022) 107090.
[5] S. Li, Dynamic responses of unsaturated ground with or without embankment under moving loads using 2.5D FEM with perfectly match layer, Geomech. Geoengin. 17 (5) (2022) 1594–1617.
[6] L. Andersen, C. Jones, Coupled boundary and finite element analysis of vibration from railway tunnels - A comparison of two- and three-dimensional models, J. Sound Vib. 293 (3–5) (2006) 611–625.
[7] P. Galvín, S. François, M. Schevenels, E. Bongini, G. Degrande, G. Lombaert, A 2.5D coupled FE-BE model for the prediction of railway induced vibrations, Soil Dyn. Earthq. Eng. 30 (12) (2010) 1500–1512.
[8] G.-Y. Gao, Q. Chen, J. He, F. Liu, Investigation of ground vibration due to trains moving on saturated multi-layered ground by 2.5D finite element method, Soil Dyn. Earthq. Eng. 40 (2012) 87–98.
[9] X. Zhang, D.J. Thompson, Q. Li, D. Kostovasilis, M.G. Toward, G. Squicciarini, J. Ryue, A model of a discretely supported railway track based on a 2.5D finite element approach, J. Sound Vib. 438 (2019) 153–174.
[10] D.J. Thompson, G. Kouroussis, E. Ntotsios, Modelling, simulation and evaluation of ground vibration caused by rail vehicles, Veh. Syst. Dyn. 57 (7) (2019) 936–983.
[11] C. Sinclair, S. Greenhalgh, B. Zhou, 2.5D modelling of elastic waves in transversely isotropic media using the spectral element method, Explor. Geophys. 38 (4) (2007) 225–234.
[12] Q. Jin, D.J. Thompson, D.E. Lurcock, M.G. Toward, E. Ntotsios, A 2.5D finite element and boundary element model for the ground vibration from trains in tunnels and validation using measurement data, J. Sound Vib. 422 (2018) 373–389.
[13] P. Amado-Mendes, P.A. Costa, L.M. Godinho, P. Lopes, 2.5D MFS–FEM model for the prediction of vibrations due to underground railway traffic, Eng. Struct. 104 (2015) 141–154.
[14] S. Zhou, C. He, P. Guo, F. Yu, Dynamic response of a segmented tunnel in saturated soil using a 2.5-D FE-BE methodology, Soil Dyn. Earthq. Eng. 120 (2019) 386–397.
[15] C. He, S. Zhou, P. Guo, H. Di, X. Zhang, Modelling of ground vibration from tunnels in a poroelastic half-space using a 2.5-D FE-BE formulation, Tunn. Undergr. Space Technol. 82 (2018) 211–221.
[16] D. Beskos, T. Krauthammer, I. Vardoulakis (Eds.), Dynamic Soil–Structure Interaction, A. A. Balkema, 1984.
[17] J. Luco, H. Wong, Seismic response of foundations embedded in a layered half-space, Earthq. Eng. Struct. Dyn. 15 (1987) 233–247.

[18] J.-F. Lu, D.-S. Jeng, S. Williams, A 2.5-D dynamic model for a saturated porous medium. Part II: Boundary element method, Int. J. Solids Struct. 45 (2) (2008) 359–377.
[19] M. Mazzotti, I. Bartoli, A. Marzani, E. Viola, A 2.5 D boundary element formulation for modeling damped waves in arbitrary cross-section waveguides and cavities, J. Comput. Phys. 248 (2013) 363–382.
[20] S. François, M. Schevenels, G. Lombaert, P. Galvín, G. Degrande, A 2.5D coupled FE-BE methodology for the dynamic interaction between longitudinally invariant structures and a layered halfspace, Comput. Methods Appl. Mech. Engrg. 199 (23–24) (2010) 1536–1548.
[21] T. Deng, M. Li, S. Zhang, X. Sheng, D.J. Thompson, Combining the 2.5D FE-BE method and the TMM method to study the vibro-acoustics of acoustically treated rib-stiffened panels, J. Sound Vib. 493 (2021) 115825.
[22] J. Huang, X. Wei, Z. Ding, W. Xu, Research on the dynamic behavior of transversely isotropic saturated media due to meeting subway loads using an improved 2.5D FE-BE method, Soil Dyn. Earthq. Eng. 191 (2025) 109244.
[23] A. Tadeu, J. António, Green's functions for 2.5D elastodynamic problems in a free solid layer formation, Eng. Struct. 24 (4) (2002) 491–499.
[24] J.-F. Lu, D.-S. Jeng, S. Williams, A 2.5-D dynamic model for a saturated porous medium: Part I. Green's function, Int. J. Solids Struct. 45 (2) (2008) 378–391.
[25] C.A. Brebbia, J. Domínguez, Boundary Elements: An Introductory Course, WIT Press, 1994.
[26] J. Domínguez, Boundary Elements in Dynamics, Computational Mechanics Publications and Elsevier Applied Science, Southampton, United Kingdom, 1993.
[27] M. Bonnet, Boundary Integral Equation Methods for Solids and Fluids, John Wiley and Sons, Chichester, United Kingdom, 1995.
[28] S. Chaillat-Loseille, R. Hiptmair, O. Steinbach, Boundary element methods, Oberwolfach Rep. 17 (1) (2021) 273–376.
[29] T. Hohage, C. Lehrenfeld, J. Preuß, Learned infinite elements, SIAM J. Sci. Comput. 43 (5) (2021) A3552–A3579.
[30] Y. Yang, H. Hung, D. Chang, Train-induced wave propagation in layered soils using finite/infinite element simulation, Soil Dyn. Earthq. Eng. 23 (4) (2003) 263–278.
[31] K. Lin, H. Hung, J.P. Yang, Y. Yang, Seismic analysis of underground tunnels by the 2.5D finite/infinite element approach, Soil Dyn. Earthq. Eng. 85 (2016) 31–43.
[32] L. Demkowicz, J. Shen, A few new (?) facts about infinite elements, Comput. Methods Appl. Mech. Engrg. 195 (29–32) (2006) 3572–3590.
[33] H.N. Gharti, W. Eaton, J. Tromp, Spectral-infinite-element simulations of seismic wave propagation in self-gravitating, rotating 3-D earth models, Geophys. J. Int. 235 (3) (2023) 2671–2693.
[34] F. Pled, C. Desceliers, Review and recent developments on the perfectly matched layer (PML) method for the numerical modeling and simulation of elastic wave propagation in unbounded domains, Arch. Comput. Methods Eng. 29 (1) (2022) 471–518.
[35] J.-P. Berenger, A perfectly matched layer for the absorption of electromagnetic waves, J. Comput. Phys. 114 (2) (1994) 185–200.
[36] S. François, M. Schevenels, G. Lombaert, G. Degrande, A 2.5D displacement based PML for elastodynamic wave propagation, Internat. J. Numer. Methods Engrg. 90 (7) (2012) 819–837.
[37] G. Rieckh, W. Kreuzer, H. Waubke, P. Balazs, A 2.5 D-fourier-BEM model for vibrations in a tunnel running through layered anisotropic soil, Eng. Anal. Bound. Elem. 36 (6) (2012) 960–967.
[38] V. Druskin, M. Guddati, T. Hagstrom, On generalized discrete PML optimized for propagative and evanescent waves, 2012, arXiv preprint arXiv:1210.7862.
[39] J. Roden, S. Gedney, Convolution PML (CPML): An efficient FDTD implementation of the CFS-PML for arbitrary media, Microw. Opt. Technol. Lett. 27 (5) (2000) 334–338.
[40] D. Appelö, G. Kreiss, A new absorbing layer for elastic waves, J. Comput. Phys. 215 (2) (2006) 642–660.
[41] F.H. Drossaert, A. Giannopoulos, A nonsplit complex frequency-shifted PML based on recursive integration for FDTD modeling of elastic waves, Geophysics 72 (2) (2007) T9–T17.
[42] M. Kuzuoglu, R. Mittra, Frequency dependence of the constitutive parameters of causal perfectly matched anisotropic absorbers, IEEE Microw. Guid. Wave Lett. 6 (12) (1996) 447–449.
[43] D. Correia, J.-M. Jin, Performance of regular PML, CFS-PML and second-order PML for waveguide problems, Microw. Opt. Technol. Lett. 48 (10) (2006) 2121–2126.
[44] S. François, H. Goh, L. Kallivokas, Non-convolutional second-order complex-frequency-shifted perfectly matched layers for transient elastic wave propagation, Comput. Methods Appl. Mech. Engrg. 377 (2021) 113704.
[45] S. Kucukcoban, L.F. Kallivokas, Mixed perfectly-matched-layers for direct transient analysis in 2d elastic heterogeneous media, Comput. Methods Appl. Mech. Engrg. 200 (1–4) (2011) 57–76.
[46] A. Zangeneh, S. François, G. Lombaert, C. Pacoste, Modal analysis of coupled soil–structure systems, Soil Dyn. Earthq. Eng. 144 (2021) 106645.
[47] S. van Ophem, O. Atak, E. Deckers, W. Desmet, Stable model order reduction for time-domain exterior vibro-acoustic finite element simulations, Comput. Methods Appl. Mech. Engrg. 325 (2017) 240–264.
[48] L. Gavrić, Finite element computation of dispersion properties of thin-walled waveguides, J. Sound Vib. 173 (1) (1994) 113–124.
[49] W.C. Chew, W.H. Weedon, A 3D perfectly matched medium from modified Maxwell's equations with stretched coordinates, Microw. Opt. Technol. Lett. 7 (13) (1994) 599–604.
[50] J.S. Hesthaven, On the analysis and construction of perfectly matched layers for the linearized Euler equations, J. Comput. Phys. 142 (1) (1998) 129–147.
[51] F. Collino, C. Tsogka, Application of the perfectly matched absorbing layer model to the linear elastodynamic problem in anisotropic heterogeneous media, Geophysics 66 (1) (2001) 294–307.
[52] R. Shi, S. Wang, J. Zhao, An unsplit complex-frequency-shifted PML based on matched Z-transform for FDTD modelling of seismic wave equations, J. Geophys. Eng. 9 (2) (2012) 218–229.
[53] U. Basu, A. Chopra, Perfectly matched layers for transient elastodynamics of unbounded domains, Internat. J. Numer. Methods Engrg. 59 (2004) 1039–1074.
[54] M. Schevenels, S. François, G. Degrande, EDT: An ElastoDynamics Toolbox for MATLAB, Comput. Geosci. 35 (8) (2009) 1752–1754.